

See discussions, stats, and author profiles for this publication at: <https://www.researchgate.net/publication/322478251>

Computed Torque Control of a Medical Parallel Manipulator

Technical Report · December 2017

CITATIONS

0

READS

1,124

1 author:



Canberk Suat Gurel

University of Maryland, College Park

10 PUBLICATIONS 4 CITATIONS

SEE PROFILE

Some of the authors of this publication are also working on these related projects:



Control of a Medical Parallel Manipulator [View project](#)



Hexapod Modelling, Path Planning and Control [View project](#)

Computed Torque Control of a Medical Parallel Manipulator

APPLIED TO CARDIOPULMONARY RESUSCITATION

CANBERK SUAT GUREL
UID: 115595972

Abstract

In practice, during cardiopulmonary resuscitation, the rescuer places the left hand on top of the right hand and uses his/her body weight to apply compressions to the middle of the chest. This configuration of hands constitutes a parallel mechanism, which inspired the mechanical design of the medical parallel manipulator that is presented in this paper. Inverse dynamics model of the parallel manipulator is derived using the principle of virtual work and the human chest is modeled as a spring-damper system. During the chest compression motion, the parallel manipulator tracks a trajectory. This paper presents a dynamic control methodology using computed torque method to control the motion of the robot manipulator. The proposed medical parallel manipulator is modeled using a multi-domain modeling and simulation tool, *MapleSim*. The modeled manipulator performed CPR to the human chest model in the *MapleSim* environment and the results regarding the performance of the control algorithm are presented.

Keywords: Medical robots, parallel manipulators, inverse dynamics

Table of Contents

ABSTRACT	1
TABLE OF CONTENTS	2
1. INTRODUCTION	3
2. KINEMATIC ANALYSIS	6
I. PROPOSED CONCEPTUAL DESIGN	6
II. INVERSE KINEMATICS	8
III. JACOBIAN MATRIX.....	10
IV. WORKSPACE	10
3. DYNAMIC ANALYSIS.....	11
I. DYNAMIC MODELING OF 3-RRPAR MEDICAL MANIPULATOR.....	11
II. MECHANICAL MODELING OF HUMAN CHEST	13
4. CONTROL OF THE NOVEL PARALLEL MANIPULATOR	16
I. COMPUTED TORQUE CONTROL USING PD CONTROLLER	16
5. SIMULATION RESULTS	18
I. 3-RRPAR MEDICAL MANIPULATOR.....	18
II. MECHANICAL HUMAN CHEST	20
III. 3-RRPAR MEDICAL MANIPULATOR APPLIED TO A MECHANICAL HUMAN CHEST.....	22
6. CONCLUSION	25
7. REFERENCES	26
8. APPENDIX.....	28
I. ADDITIONAL VISUALS OF THE PROPOSED DESIGN.....	28
II. DETAILED INVERSE KINEMATICS CALCULATIONS.....	29
III. SIMPLIFICATION HYPOTHESIS	31
IV. YOUTUBE VIDEO	31
V. <i>MAPLESIM</i> AND <i>SOLIDWORKS</i> FILES	31

1. Introduction

Cardiopulmonary resuscitation (CPR) is the procedure that is applied when a person is in cardiac arrest. This procedure typically consists of chest compression, chest decompression and artificial ventilation. The main intension is to replace the hearths rhythm, restore partial blood circulation and hence gain the patient a brief amount of time until he/she receives an electric shock to restart the heart.

For an adult, the chest compressions should be delivered at a rate of at least 100 compressions per minute with the depth of 4 to 5 cm [1]. In the case of a patient being in cardiac arrest, typically, the patient has approximately 5 to 6 minutes until permanent tissue and brain damage or death occurs [2]. A study by American Heart Association revealed that the chances of survival of a patient suffering from cardiac arrest declines by 7-10% for every minute of delay until CPR is applied [3]. Hence, the timely application of CPR plays a vital role in the survival of the patient.

The proposed medical parallel manipulator may be a good alternative to manual chest compression for three main reasons. First, the changes in speed of a dynamic environment such as an ambulance causes instability due to inertia and downgrades the quality of the chest compressions that the patient receives. Second, some patients may be infected by indeterminate diseases, which may transmit to the doctor performing CPR. SARS corona virus is an example to such diseases that could not be identified until recently. A number of doctors performing CPR to a patient were transmitted with SARS corona virus [4]. Third, manual chest compression consumes a lot of energy from doctors and it is often a tradeoff between the number of doctors circulating and the quality of CPR during the cases requiring continuous chest compression. An example was given by [5] where 10 doctors circulated to perform chest compression for 2 hours, which demonstrates that these doctors could better use their valuable time with the chest compression assistive medical robot.

A parallel manipulator is a closed-loop kinematic chain mechanism whose end-effector (the mobile platform) is connected to the fixed base by several independent kinematic chains in parallel [6]. Figure 1 demonstrates some of the commonly used parallel manipulator types.

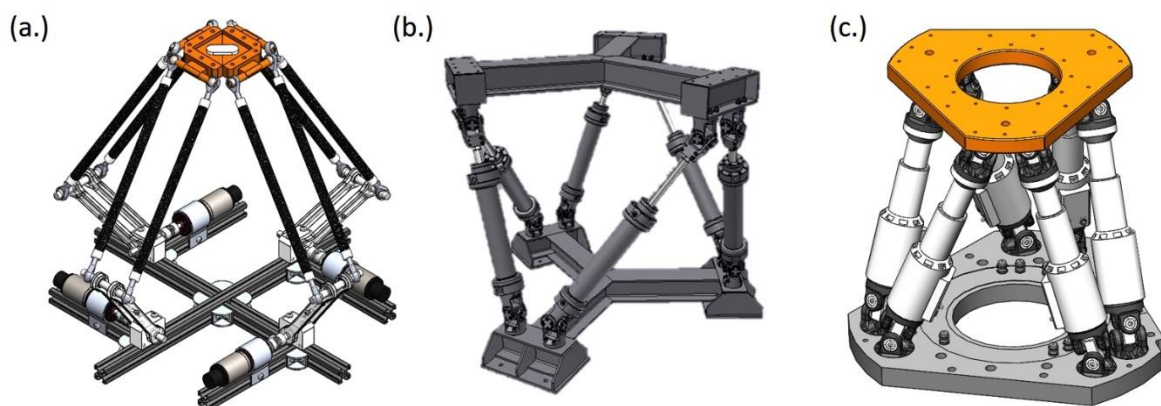


Figure 1: Different types of parallel manipulator configurations

Figure 1 (a.) is the 4 DOF Delta type parallel manipulator, unlike the other two, it consists of revolute joints. Figure 1 (b.) is the hexapod parallel manipulator, which is commonly used for

manufacturing, inspection and research [6]. Figure 1 (c.) is a 6 DOF parallel platform named after its inventor D. Steward, who proposed this design in 1965 for flight simulators [7].

Figure 2 shows the two industrial manipulators developed by ABB, (a.) IRB 940 Triceps and (b.) IRB 360 FlexPicker. The IRB 940 Triceps robot is designed for cleaning and pre-machining of heavy aluminum castings [8]. The robot weighs 580 kg and is capable of carrying a maximum payload of 40 kg [8]. The IRB 360 FlexPicker robot is a high-speed pick and place robot, which is often used in production lines. The integrated vision software allows the robot to detect and relocate objects reaching up to 8 kg [9]. For instance, Müller Dairy installed IRB 360 FlexPicker robots in their new repacking lines; the new system is not only 50% more efficient but also repacks 420 pots per minute, which is double the number of pots repacked manually [10].

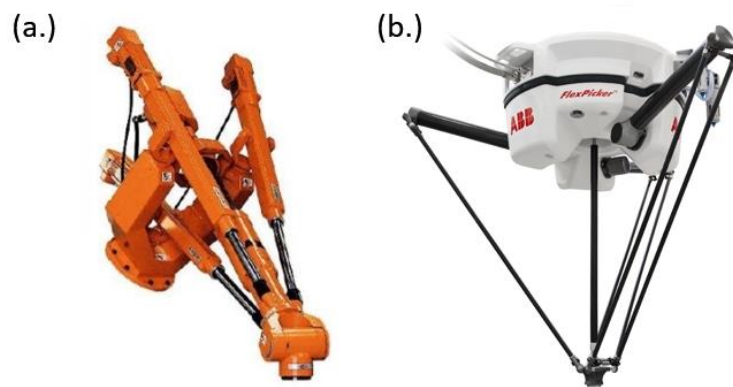


Figure 2: Industrial parallel manipulators developed by ABB

Parallel manipulators possess a tremendous potential of applications in the field of medical robotics due to their intrinsically high stiffness, high accuracy, high speed, and high load carrying capability advantages over their serial counterparts [5]. The main disadvantage of parallel manipulators is the limited workspace of the end-effector [5]. Besides the limited workspace, the kinematics of the parallel manipulators is considered challenging to analyze.

The proposed 3-RRPaR manipulator is an alternative to chest compression in the process of classical CPR. A number of other alternatives to classical CPR are presented in [11]. Figure 3 shows the alternative methods to classical CPR. Figure 3 (a.) is the active compression-decompression (ACD) CPR method that is applied using a plunger-like device with an integral suction cup. This device allows for the decompression of the chest between successive compressions. Figure 3 (b.) is the interposed abdominal compression (IAC) CPR method that requires at least two people to apply recursive compressions to both abdominal and chest, which is proven to increase the blood flow into the chest. Figure 3 (c.) is a 4 phase method that is a combination of the ACD and IAC CPR methods. It is applied using an equipment called *lifestick*. Figure 3 (d.) is the vest CPR method. In this method, a vest wraps the chest around and the attached pneumatic system pumps air in and out the vest causing a circumferential compression, which replicates the inhalation and exhalation stages of the chest. Figure 3 (e.) is the piston chest compression (PCR) method. The piston applies vertical compressions to the chest, in this sense the PCR method is similar to the 3-RRPaR manipulator proposed in this paper.

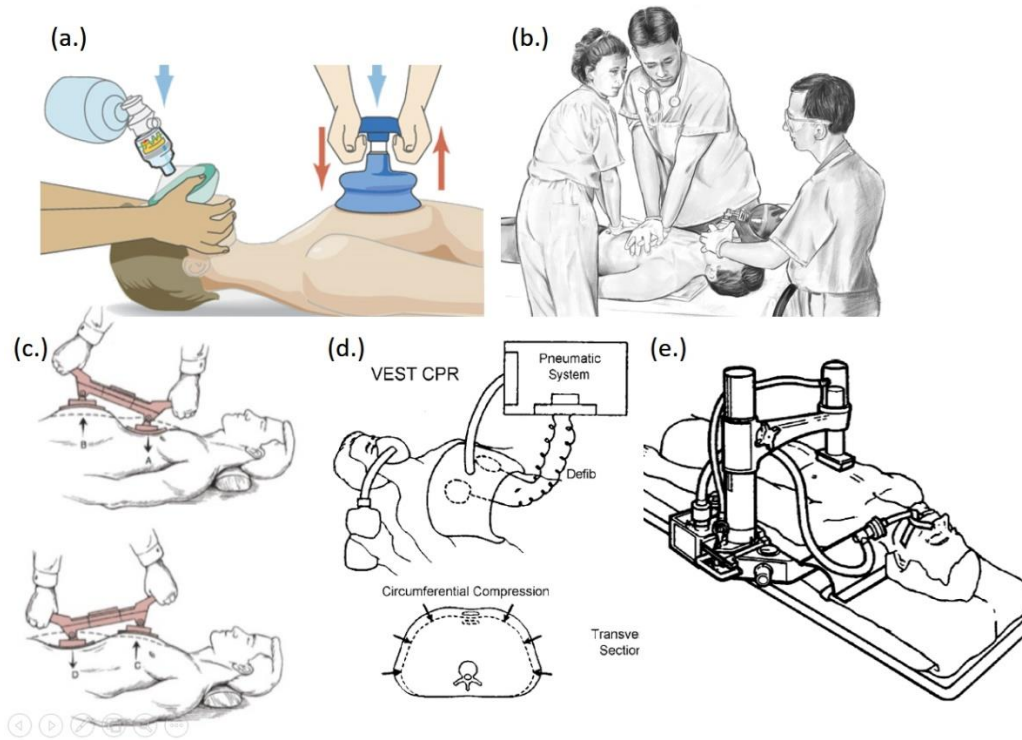


Figure 3: Five alternatives to classical CPR, adapted from [11]

The paper is organized as follows, in Section 2; the proposed design of the robot manipulator is described in detail, inverse kinematics equations of the manipulator are derived and using the derived inverse kinematic equations, the reachable workspace of the 3-RRPaR manipulator is visualized. In Section 3, the dynamic model of the 3RRPaR manipulator is derived making use of the principle of virtual work, then the human chest is modeled as a spring-damper system. The inverse dynamics control methodology that was implemented in the given dynamic model is presented in Section 4. In Section 5, the 3RRPaR manipulator is simulated in the *MapleSim* environment and the obtained simulation results are represented. Finally, the paper is concluded in Section 6 with a few final remarks and potential future work to be done.

2. Kinematic Analysis

In this chapter, the kinematics of the 3RRPaR manipulator is described, which focuses on the geometry of the robot motion by neglecting the forces and torques that involve in the motion.

i. Proposed Conceptual Design

During cardiopulmonary resuscitation (CPR), the rescuer places the left hand on top of the right hand and uses his/her body weight to apply compressions to the middle of the chest. Figure 4 shows a person performing CPR. This configuration of hands constitutes a parallel mechanism, which inspired the mechanical design of the medical parallel manipulator that is presented in this paper.

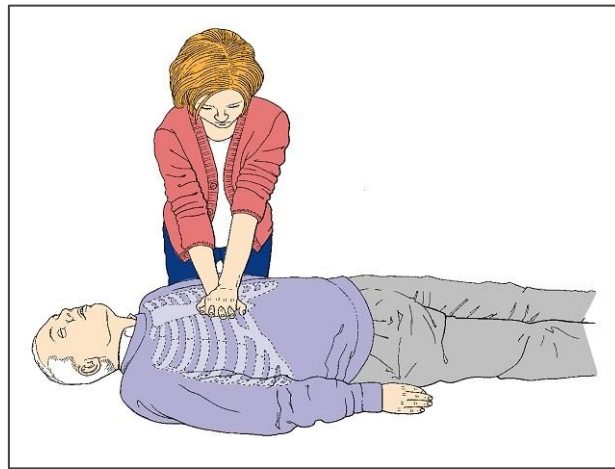


Figure 4: Chest compression operation in CPR, adapted from [12]

The CPR parallel manipulator that is shown in Figure 5 is from the Delta family; however, unlike the 4-DOF parallel manipulator shown in Figure 1 (a.), the proposed design has only three revolute joints. This design choice increased the complexity. Since the axis of rotation of the actuators are no longer perpendicular to each other, equilateral triangles needed to be considered while creating the model for simulations presented in Chapter 5. However, in return, the use of one fewer actuator reduced the costs and hence turned the design into a financially more feasible solution for hospitals.

Figure 5 illustrates the proposed design of the CPR assistive 3-RRPaR manipulator, where a patient lies down on a stretcher and the CPR robot is positioned on top of the patient's chest. In the CPR operation, the mobile platform of the robot needs to translate vertically in Z-axis. However, the mobile platform is also capable of moving in X and Y axes, which allows the doctors to position the mobile platform to a suitable position during the CPR operation [13]. The CPR assistive 3RRPaR manipulator is mounted underneath a height adjustable base; the magnified view demonstrates the pulleys enclosed inside the two supporting columns. Since the supporting columns carry the weight of the fixed base and the three actuators, the weight of the actuators do not impose a disturbance on the moving parts of the manipulator. The entire system is light enough to be moved around by a single person, minimizing the response time to the patient, who is racing against time. A slightly different design is presented by [5], which occupies only one side of the stretcher and hence allows easier

access to the patient. The additional visuals of the proposed 3RRPaR manipulator design are provided in **Appendix**.

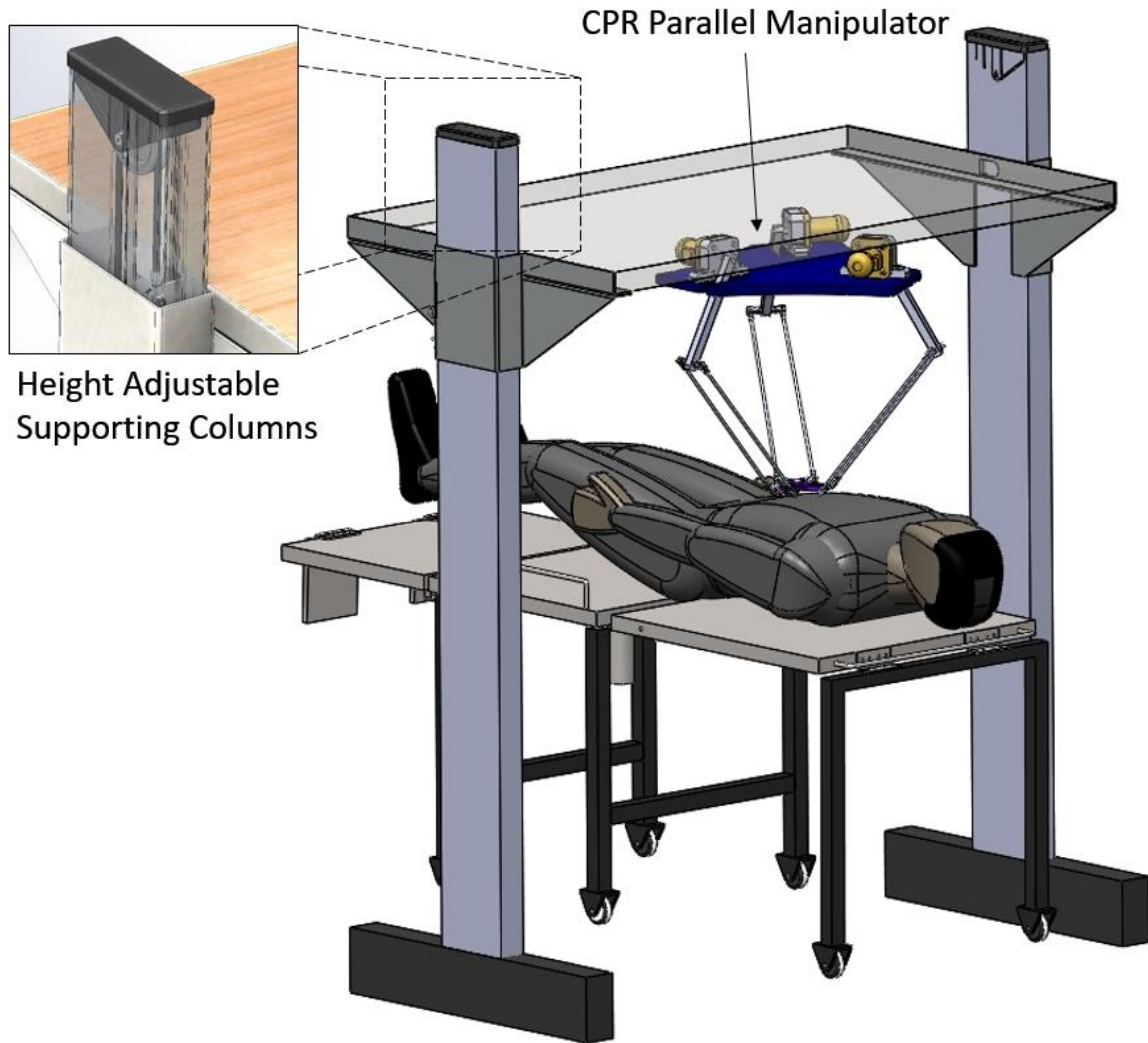


Figure 5: SolidWorks design of the Delta type CPR parallel manipulator

The CPR assistive parallel manipulator shown in Figure 6 (a.) consists of a fixed base, a mobile platform (end-effector), and 3 sets of 3 revolute joints (R) and parallelogram (Pa) pairs [14]. Taking the order of the three revolute joints and the parallelogram into account, the medical manipulator is called as 3-RRPaR manipulator. Figure 6 (b.) demonstrates the simplified representation of the designed 3-RRPaR manipulator. Following [14], point O and point P denote the origin of the fixed frame $O\{x, y, z\}$ and the origin of the moving frame $P\{u, v, \omega\}$, respectively. Point $A_i, i \in \{1, 2, 3\}$ denotes the position of three actuators. Point $B_i, i \in \{1, 2, 3\}$ denotes the universal joints between the upper and the lower links, with the length a and b , respectively. Point $C_i, i \in \{1, 2, 3\}$ denotes the point of connection of the moving platform and the lower links.

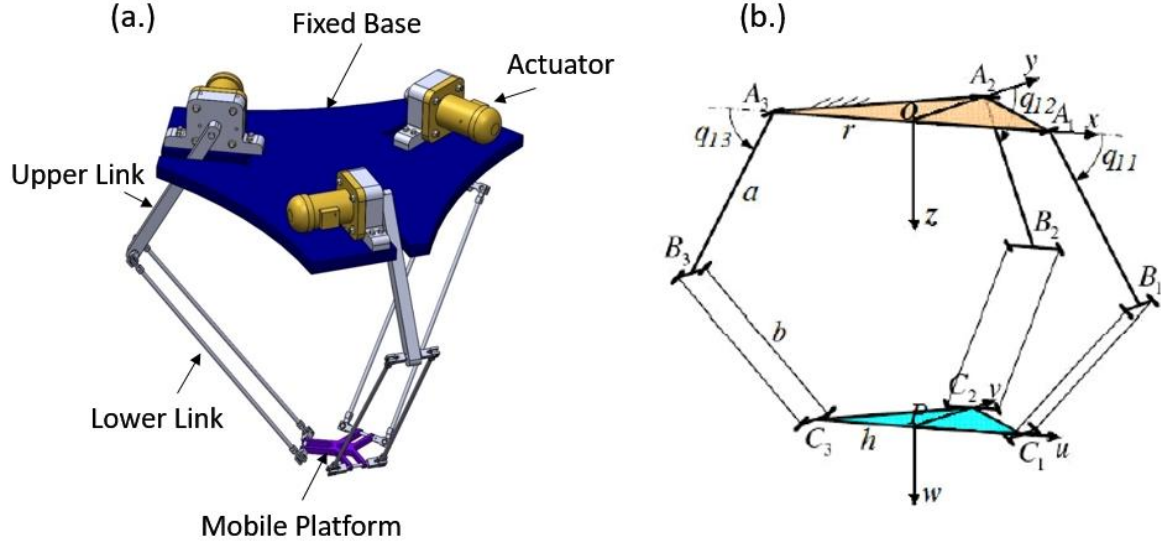


Figure 6: The designed CPR parallel manipulator and the simplified schematic representation

Parameter	Value	Unit
r	160	mm
a	200	mm
b	200	mm
h	120	mm

Table 1: Dimensions of the simplified schematic representation [14]

ii. Inverse Kinematics

In this section, the inverse kinematics of the 3-RRPaR manipulator is analyzed by applying the loop-closure equation method. The main objective is to express the joint angles q_{1i} , q_{2i} , and q_{3i} in terms of the position vector $p = [p_x \ p_y \ p_z]^T$, which denotes the position of the mobile platform.

Figure 7 illustrates the joint angles q_{1i} , q_{2i} , and q_{3i} . The coordinate system (x_i, y_i, z_i) is attached to the fixed base at point A_i . The angle between x axis and x_i is denoted by ϕ_i , which is a constant parameter.

Figure 7: Schematic of the simplified representation

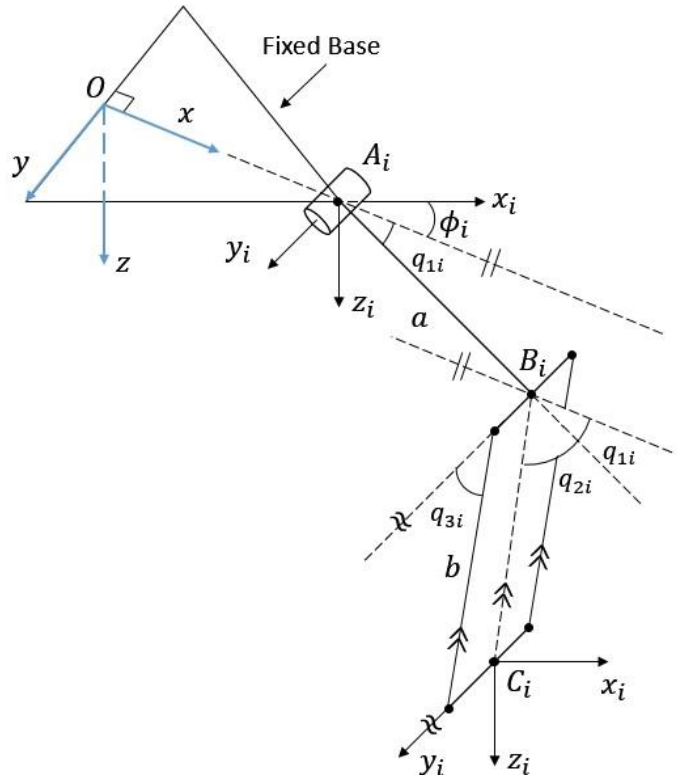


Figure 8 (a.) and (b.) show the $x_i - z_i$ plane and $y_i - z_i$ plane of Figure 7.

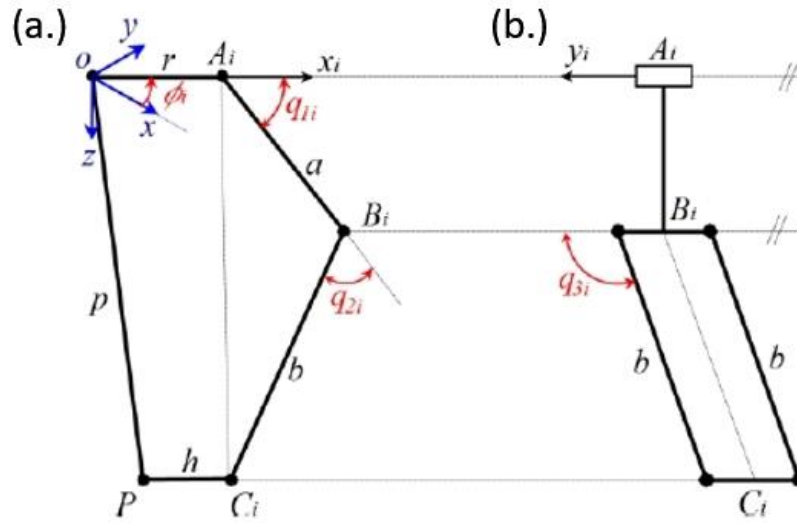


Figure 8: Plane View of Figure 7, adapted from [14]

Following [14], the loop-closure equation method is applied to Figure 8 (a.),

$$\overline{A_i C_i} = \overline{A_i B_i} + \overline{B_i C_i} = \overline{AO} + \overline{OP} + \overline{P C_i} \quad (2.1)$$

Expressing Equation 2.1 in Matrix from,

$$\begin{bmatrix} a \cos(q_{1i}) + b \sin(q_{3i}) \cos(q_{1i} + q_{2i}) \\ b \cos(q_{3i}) \\ a \cos(q_{1i}) + b \sin(q_{3i}) \sin(q_{1i} + q_{2i}) \end{bmatrix} = \begin{bmatrix} Cx_i \\ Cy_i \\ Cz_i \end{bmatrix} \quad (2.2)$$

where

$$\begin{bmatrix} Cx_i \\ Cy_i \\ Cz_i \end{bmatrix} = \begin{bmatrix} \cos(\phi_i) & \sin(\phi_i) & 0 \\ -\sin(\phi_i) & \cos(\phi_i) & 0 \\ 0 & 0 & 1 \end{bmatrix} \begin{bmatrix} p_x \\ p_y \\ p_z \end{bmatrix} + \begin{bmatrix} h - r \\ 0 \\ 0 \end{bmatrix} \quad (2.3)$$

Combining Equations 2.2 and 2.3 yields 3 simultaneous equations:

$$a \cos(q_{1i}) + b \sin(q_{3i}) \cos(q_{1i} + q_{2i}) = \cos(\phi_i) p_x + \sin(\phi_i) p_y + h - r \quad (2.4)$$

$$b \cos(q_{3i}) = -\sin(\phi_i) p_x + \cos(\phi_i) p_y \quad (2.5)$$

$$a \cos(q_{1i}) + b \sin(q_{3i}) \sin(q_{1i} + q_{2i}) = p_z \quad (2.6)$$

Solving Equation 2.5 for q_{3i} ,

$$q_{3i} = \pi - \cos^{-1} \left(\frac{\sin(\phi_i) p_x - \cos(\phi_i) p_y}{b} \right) \quad (2.7)$$

Calculating the sum of squares of Equations 2.4, 2.5 and 2.6 it is possible to determine q_{2i} . The detailed calculation steps can be found in **Appendix**.

The sum of squares of the RHS is

$$p_x^2 + p_y^2 + p_z^2 + 2(h - r)(\cos(\phi_i) p_x + \sin(\phi_i) p_y) + (h - r)^2 \quad (2.8)$$

The sum of squares of the LHS is

$$a^2 + 2ab \sin(q_{3i}) \cos(q_{2i}) + b^2 \quad (2.9)$$

Equating Equations 2.8 and 2.9, q_{2i} is given as,

$$q_{2i} = \cos^{-1} \left(\frac{\text{Equation 2.8} - a^2 - b^2}{2ab \sin(q_{3i})} \right) \quad (2.10)$$

Substituting Equations 2.7 and 2.10 into Equation 2.2, each solution of q_{2i} and q_{3i} yields a unique solution of q_{1i} . As a result, the joint angles q_{1i} , q_{2i} , and q_{3i} are defined in terms of the position of the mobile platform.

iii. Jacobian Matrix

The Jacobian matrix J of the parallel manipulator is given in [13]. It should be noted that as the proposed parallel manipulator design has 3 DOF, the J is a 6×3 matrix. Since the J is not square, the Moore-Penrose pseudoinverse method needs to be used for calculating J^{-1} . MATLAB command `pinv(J)` returns the pseudoinverse of J .

iv. Workspace

The high-stiffness and high-accuracy properties of parallel manipulators makes this design a suitable alternative to manual chest compression, however it is worth noting that the main disadvantage of the parallel manipulators is the limited workspace that they provide [5].

Figure 9 demonstrates the workspace of the 3-RRPaR manipulator that was located in the origin. The plot is color coded, where red and blue demonstrate the highest and lowest positions that the manipulator is capable of reaching, respectively.

The parallel manipulator is capable of satisfying a vertical displacement of 30 cm. Although the workspace of the proposed parallel manipulator is fairly limited, the manipulator satisfies the requirements for the CPR operation, which requires a vertical motion of 4 to 5 cm.

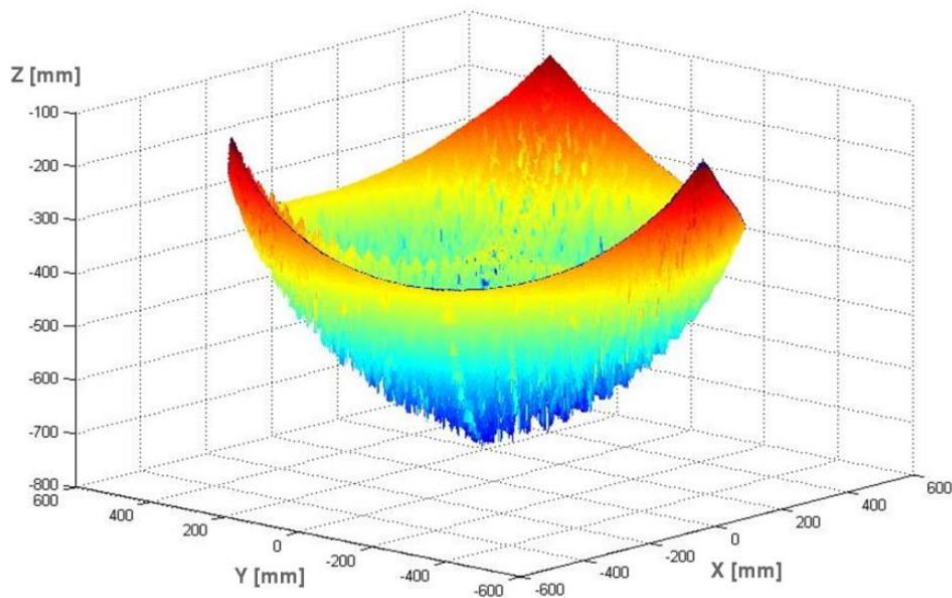


Figure 9: The Workspace of the 3RRPaR Manipulator

3. Dynamic Analysis

i. Dynamic Modeling of 3-RRPaR Medical Manipulator

A number of simplification hypothesis needed to be employed in order to simplify the dynamic problem of the 3-RRPaR manipulator, without losing the generality of the model. The simplification hypotheses are provided in **Appendix**.

Let m_a , m_b , and m_p denote the mass of upper link A_iB_i , each lower link B_iC_i , and the moving platform, respectively. The numeric values of masses are given by Table 2.

Components of Parallel Manipulator	Letter Representation	Mass	Value (kg)
Upper Link A_iB_i	a	m_a	0.3
Lower Link B_iC_i	b	m_b	0.1
Mobile Platform	p	m_p	0.4

Table 2: Masses of the components of parallel manipulator

Then, $\hat{m}_p = m_p + 3m_b$ and $\hat{m}_a = m_a + \frac{1}{2}m_b$ are the equivalent masses of mobile platform and upper link, respectively.

Let $\tau = [\tau_1 \ \tau_2 \ \tau_3]^T$ be the vector of actuator torques, $\delta q = [\delta q_{11} \ \delta q_{12} \ \delta q_{13}]^T$ be the vector of virtual angular displacements of joints 1, 2, and 3 and let $\delta p = [\delta p_x \ \delta p_y \ \delta p_z]^T$ be the vector of virtual linear displacement of the mobile platform. Following the procedure presented in [13], it is possible to derive Equation 3.1 by applying the principle of virtual work and neglecting the forces of friction and external disturbance.

$$\tau^T \delta q + M_{Ga}^T \delta q - M_a^T \delta q + F_{Gp}^T \delta p - F_p^T \delta p = 0 \quad (3.1)$$

where,

$$M_{Ga} = \hat{m}_a g a \begin{bmatrix} q_{11} & 0 & 0 \\ 0 & q_{12} & 0 \\ 0 & 0 & q_{13} \end{bmatrix} \quad (3.2)$$

is the vector of gravity torques of the upper links and

$$F_{Gp} = \hat{m}_p [0 \ 0 \ -g]^T \quad (3.3)$$

is the vector of gravity force of the mobile platform, where g is the acceleration due to gravity. The vector of inertia torques of the upper links M_a is given as,

$$M_a = \hat{I}_a \ddot{q} = \hat{I}_a [\dot{q}_{11} \ \dot{q}_{12} \ \dot{q}_{13}]^T \quad (3.4)$$

where, the inertia matrix of the uppers links is given as,

$$\hat{I}_a = a^2 \hat{m}_a I \quad (3.5)$$

where, I denotes a 3×3 identity matrix. The vector of inertia forces of the mobile platform is given as,

$$F_p = \hat{M}_p \ddot{p} = \hat{m}_p \begin{bmatrix} \ddot{p}_x & 0 & 0 \\ 0 & \ddot{p}_y & 0 \\ 0 & 0 & \ddot{p}_z \end{bmatrix} \quad (3.6)$$

Following the unit textbook [15], the relationship between the end-effector velocity ξ and the joint velocities \dot{q} is given as

$$\xi = J \dot{q} \quad (3.7)$$

where J is the Jacobian matrix.

The joint angle configurations q and velocities \dot{q} are denoted as

$$q = [q_{11} \quad q_{12} \quad q_{13}]^T \quad (3.8)$$

and

$$\dot{q} = [\dot{q}_{11} \quad \dot{q}_{12} \quad \dot{q}_{13}]^T \quad (3.9)$$

respectively. Making the assumption that the Jacobian matrix is non-singular and square, J matrix can be inverted and hence

$$\dot{q} = J^{-1} \xi \quad (3.10)$$

In our case, the notation of p is used for linear displacement of the end-effector. Therefore, the end-effector velocity ξ is given as,

$$\xi = \dot{p} = [\dot{p}_x \quad \dot{p}_y \quad \dot{p}_z]^T \quad (3.11)$$

Hence, Equations 3.7 and 3.10 can be written as

$$\dot{p} = J \dot{q} \quad (3.12)$$

$$\dot{q} = J^{-1} \dot{p} \quad (3.13)$$

Differentiating Equation 3.12 with respect to time,

$$\ddot{p} = \dot{J} \dot{q} + J \ddot{q} \quad (3.14)$$

Derivative of x and q with respect to time t can be represented as the ratio of an infinitesimal change in time varying variables, p and q , and time t . Then, Equation 3.12 can be written as,

$$\delta p = J \delta q \quad (3.15)$$

Substituting Equation 3.15 into Equation 3.1,

$$(\tau^T + M_{Ga}^T - M_a^T + F_{Gp}^T J - F_p^T J) \delta q = 0 \quad (3.16)$$

The virtual displacement term can be eliminated as Equation 3.16 holds for any δq . Then, rearranging Equation 3.16 gives

$$-M_{Ga} + M_a - J^T F_{Gp} + J^T F_p = \tau \quad (3.17)$$

Substituting Equations 3.4 and 3.6 into Equation 3.17,

$$-M_{Ga} + \hat{I}_a \ddot{q} - J^T F_{Gp} + J^T \hat{M}_p \ddot{p} = \tau \quad (3.18)$$

Substituting Equation 3.14 into Equation 3.18,

$$-M_{Ga} + \hat{I}_a \ddot{q} - J^T F_{Gp} + J^T \hat{M}_p (\dot{J}\dot{q} + J\ddot{q}) = \tau \quad (3.19)$$

Following [14], the dynamic equations of the medical parallel manipulator is given as,

$$\tau = M(q)\ddot{q} + C(q, \dot{q})\dot{q} + G(q) \quad (3.20)$$

where, $M(q) \in \mathbb{R}^{3 \times 3}$ is the inertia matrix, $C(q, \dot{q}) \in \mathbb{R}^{3 \times 3}$ is the ventrifugal and Coriolis forces matrix, and $G(q) \in \mathbb{R}^3$ is the vector of gravity.

Comparing Equations 3.19 and 3.20,

$$M(q) = \hat{I}_a + J^T \hat{M}_p J$$

$$C(q, \dot{q}) = J^T \hat{M}_p \dot{J}$$

$$G(q) = -M_{Ga} - J^T F_{Gp}$$

ii. Mechanical Modeling of Human Chest

Following the procedure presented in [16], the human chest may be modeled as a mass spring-damper system. Figure 10 shows a mechanical human chest represented as a spring-damper system with stiffness k , damping μ and subjected to an external force F_t .

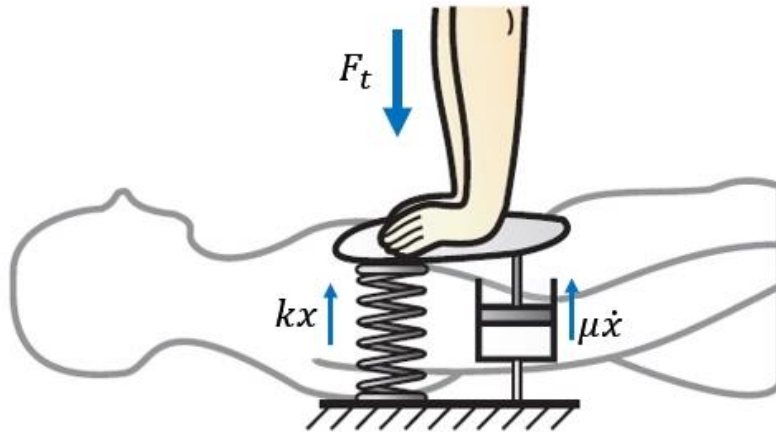


Figure 10: Compression of the mechanical chest represented as a spring-damper system

The equation of motion of the system is

$$F_t + mg = F_k + F_\mu + F_m \quad (3.21)$$

where m is the moving mass of the chest and g is the acceleration due to gravity.

The elastic force $F_k = -kx$, damping force $F_\mu = -\mu\dot{x}$, and inertia force due to moving mass $F_m = -m\ddot{x}$. Therefore, Equation 3.1 is expressed as,

$$F_t + mg = -kx - \mu\dot{x} - m\ddot{x} \quad (3.22)$$

where x denotes linear displacement of the chest.

The moving mass of the chest m is relatively small compared to stiffness k and damping μ . As a result, the inertia force F_m is relatively small compared to elastic force F_k and damping force F_μ [16]. Hence, the inertia force F_m due to the moving mass m can be neglected.

$$F_t = F_k + F_\mu \quad (3.23)$$

where stiffness k and damping coefficient μ are dependent on displacement d , hence the elastic force F_k and damping force F_μ are redefined as,

$$F_k = -k(d)x \text{ and } F_\mu = -\mu(d)\dot{x}(d)$$

Then the resulting equation of motion is given as,

$$F_t(d) = -k(d)x - \mu(d)\dot{x}(d) \quad (3.24)$$

Considering a small change in x , Equation 3.4 can be written as,

$$F_t^+(d) - F_t^-(d) = -k(d)(x^+ - x^-) - \mu(d)(\dot{x}^+(d) - \dot{x}^-(d)) \quad (3.25)$$

where (+) and (-) denote the direction of the motion, compression and decompression, respectively. Then the damping coefficient $\mu(d)$ is isolated as follows,

$$\mu(d) = \frac{F_t^+(d) - F_t^-(d)}{\dot{x}^+(d) - \dot{x}^-(d)} \quad (3.26)$$

Likewise, the stiffness $k(d)$ is isolated by choosing the (+) direction of the motion, i.e. compression.

$$k(d) = \frac{F_t^+(d) - \mu(d) \dot{x}^+(d)}{d} \quad (3.27)$$

Figure 11 (a.) shows the cross-sectional view of a spring-damper system imbedded into a human chest. Alternative to the spring-damper system, a pneumatic damper maybe used to replicate the mechanical properties of a human chest. A possible implementation of pneumatic damper is presented by [17] in order to develop a CPR training manikin, shown by Figure 11 (b.).

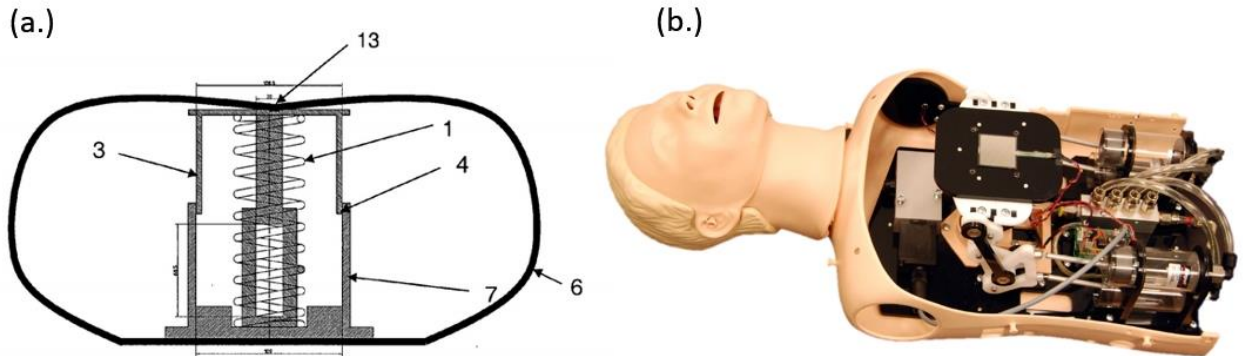


Figure 11: (a.) Spring-damper system inside human chest [18] and (b.) pneumatic damper inside a CPR training manikin [17]

Figure 12 (a.) shows the obtained depth as a result of the applied force during the compression stage of the CPR operation, in a number of experiments with real patients. The obtained plot demonstrates a parabolic envelope, which differs depending on the initial chest

height of the patient. Figure 12 (b.) shows the displacement of the chest with respect to the chest level and the force applied to the chest during manual CPR operation. The (-) sign of the relative displacement indicates that the mobile platform moves below the initial chest level. It can be seen that the applied force peaks at the transition from the compression stage to the decompression stage, reaching a maximum value of 353N. In addition, the chest displacement reached a maximum value of 4.3 cm slightly after the transition due to inertia created as a result of the change in direction of applied force.

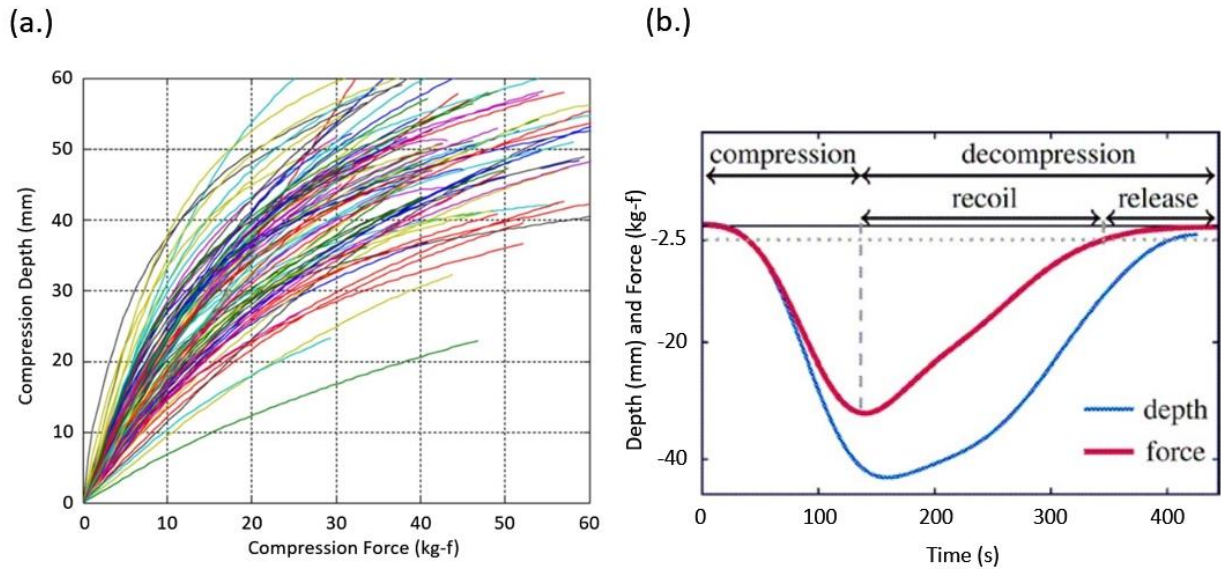


Figure 12: Displacement and Applied Force in Manual CPR, [19] [20]

Using Equations 3.6 and 3.7 it is possible to calculate the range of human chest stiffness and damping based on the data presented in Figure 12 (a.). The results are given in Table 2.

Compression Force Range (N)	Compression Depth (cm)	Chest Stiffness (N/m)	Chest Damping (Ns/m)
117-490	4	2925-12250	175-735
196-588	5	3920-11760	235-705

Table 3: Chest stiffness and damping based on Figure 12 (a.)

Figure 13 demonstrates the distribution of force that is needed to be applied in order the compression to reach the recommended depth of 53 mm. In this experiment, the range initial chest height of all the patients was between 185 mm and 305 mm, as any chest height outside this range causes a nonlinear behavior. The results of the experiment showed that the greatest portion of patients required a force within the range of 350 N and 399 N to be applied for the chest compressions to reach 53 mm below the chest level.

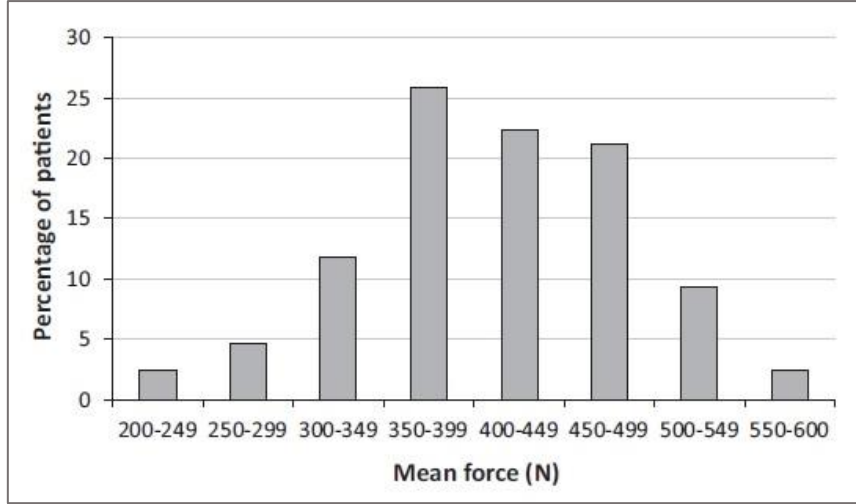


Figure 13: The mean force that needs to be applied to the patients for the compression to reach a depth of 53 mm, [21]

4. Control of the Novel Parallel Manipulator

i. Computed Torque Control using PD Controller

In this section, an implementation of inverse dynamics is presented for computing the required joint actuator torques that must be generated by the actuators to achieve a given trajectory [22].

The joint space dynamic model that was given by Equation 3.20, can be written as,

$$\tau = M(q)\ddot{q} + H(q, \dot{q}) \quad (4.1)$$

where $H(q, \dot{q}) = C(q, \dot{q})\dot{q} + G(q)$. The main idea is to seek a nonlinear feedback control law

$$\tau = f(q, \dot{q}, t) \quad (4.2)$$

which, using inverse dynamics method, results as a linear closed-loop system [15].

If the control law τ is chosen according to inverse dynamics control equation

$$\tau = M(q)a_q + H(q, \dot{q}) \quad (4.3)$$

Since the inertia matrix $M(q) \in \mathbb{R}^{3 \times 3}$ is invertible, combining Equations 4.1 and 4.3 yields,

$$\ddot{q} = a_q \quad (4.4)$$

The term a_q represents an input signal in acceleration form and since now a_q can be designed to control a linear second order system. As it is explained in [23], there are many possible choices of a_q that achieves remarkable results, one of these choices of a_q is,

$$a_q = \ddot{q}_d + K_d\dot{\tilde{q}} + K_p\tilde{q} \quad (4.5)$$

where $\tilde{q} = q_d - q$. The proportional and derivative gains of the PD controller are denoted by K_p and K_d , respectively. Substituting Equation 4.5 into Equation 4.4,

$$\ddot{q} = \ddot{q}_d + K_d\dot{\tilde{q}} + K_p\tilde{q} \quad (4.6)$$

Rearranging Equation 4.6 yields,

$$\ddot{\tilde{q}} + K_d \dot{\tilde{q}} + K_p \tilde{q} = 0 \quad (4.7)$$

A suitable choice of K_p and K_d gains will provide an improved trajectory tracking as the trajectory tracking error will asymptotically approach to zero. A possible choice of K_p and K_d is suggested by [15] as $K_p = \text{diag}\{\omega_1^2, \omega_2^2, \dots, \omega_n^2\}$ and $K_d = \text{diag}\{2\omega_1, 2\omega_2, \dots, 2\omega_n\}$, where $\omega_i \in \{1, 2, \dots, n\}$ is the natural frequency of a critically damped linear second order system. To sum up, given that suitable values of K_p and K_d were chosen, the inverse dynamics control design resulted with a linear and decoupled closed-loop system. Figure 14 demonstrates the block diagram of computed torque control using PD controller.

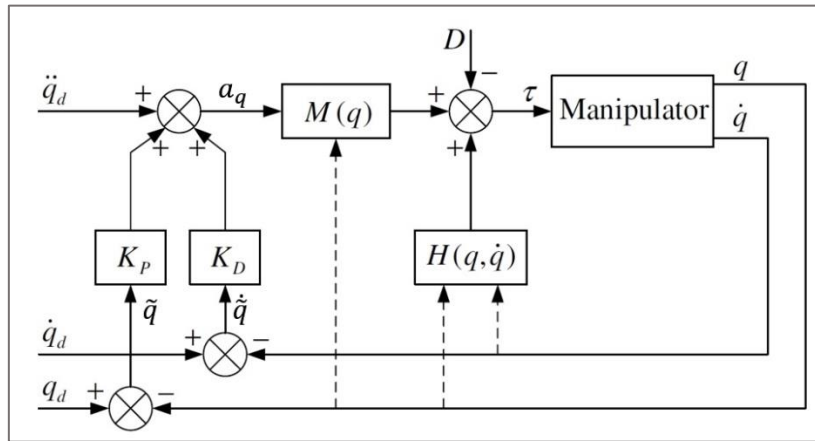


Figure 14: Block diagram of the implementation

Figure 15 shows the inner-loop / outer-loop control architecture and Figure 16 shows the Simulink implementation of this control architecture. The inner-loop, using Equation 4.3, computes the nonlinear control law τ as a function of the input signal a_q and the measured joint position q and joint velocity \dot{q} . The outer-loop is designed to compute the input signal a_q given a reference trajectory q_d . There are different methods to design an outer-loop feedback control; one of the commonly used methods makes use of Lyapunov's second method based on the theory of guaranteed stability of uncertain systems [15]. In our case, the design of outer-loop is simplified as it is designed for a linearized plant, shown by the dotted enclosure in Figure 15.

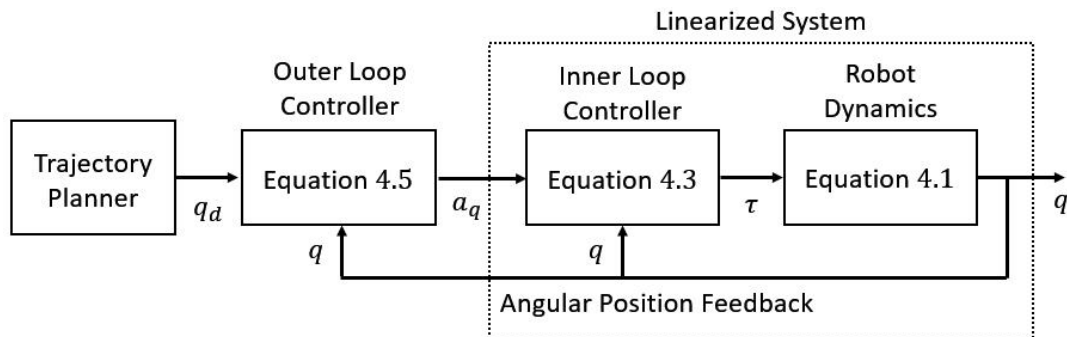


Figure 15: Inner-loop / outer-loop control architecture

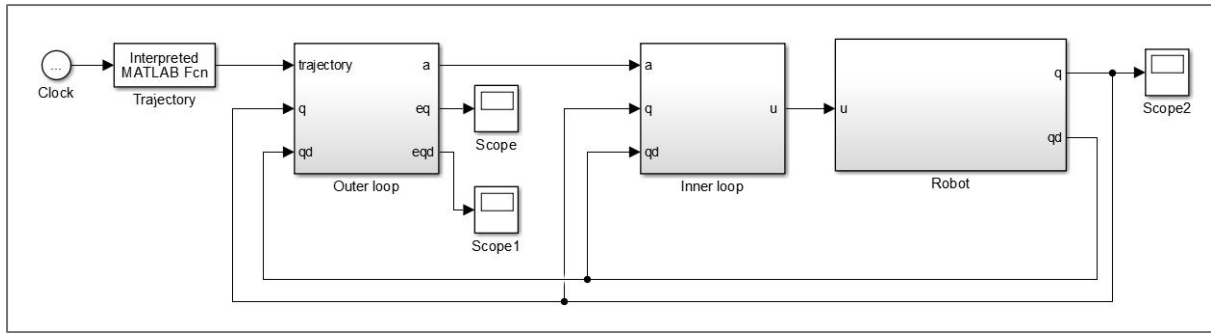


Figure 16: Inner-loop / outer-loop control architecture implementation in Simulink

The model shown by Figure 16 is provided to demonstrate how the inner-loop / outer-loop control architecture maybe implemented in the Simulink environment. This particular model was generated for the inverse dynamics control of legged-robots presented in my final year dissertation entitled *Hexapod Modelling, Path Planning and Control* [24].

5. Simulation Results

i. 3-RRPaR Medical Manipulator

The 3-RRPaR medical manipulator is modeled using the *MapleSim* software, which is an advanced system-level modeling tool developed by *Maplesoft*. The model that is shown by Figure 17 consists of three sets of 3 revolute joints and parallelogram pairs. The parallelograms are formed by using spherical joints, which restrict the relative motion of the two bodies to a pure rotation about the common origin, i.e. relative translation of the two bodies is prevented.

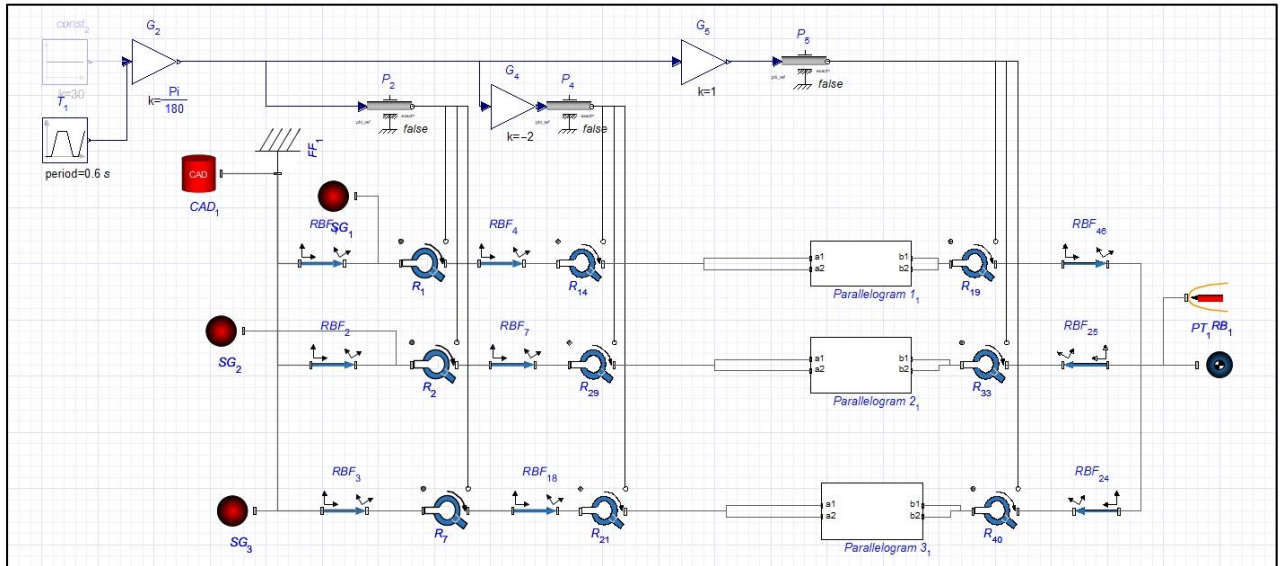


Figure 17: The MapleSim model of the 3-RRPaR medical manipulator

Figure 18 demonstrates the initial (a.) and final (b.) positions of the manipulator end-effector during the CPR operation. This result proves that the graphical code in Figure 18 compiles successfully and the model moves as anticipated. A URL link to the YouTube video showing the motion of the model is provided in **Appendix**.

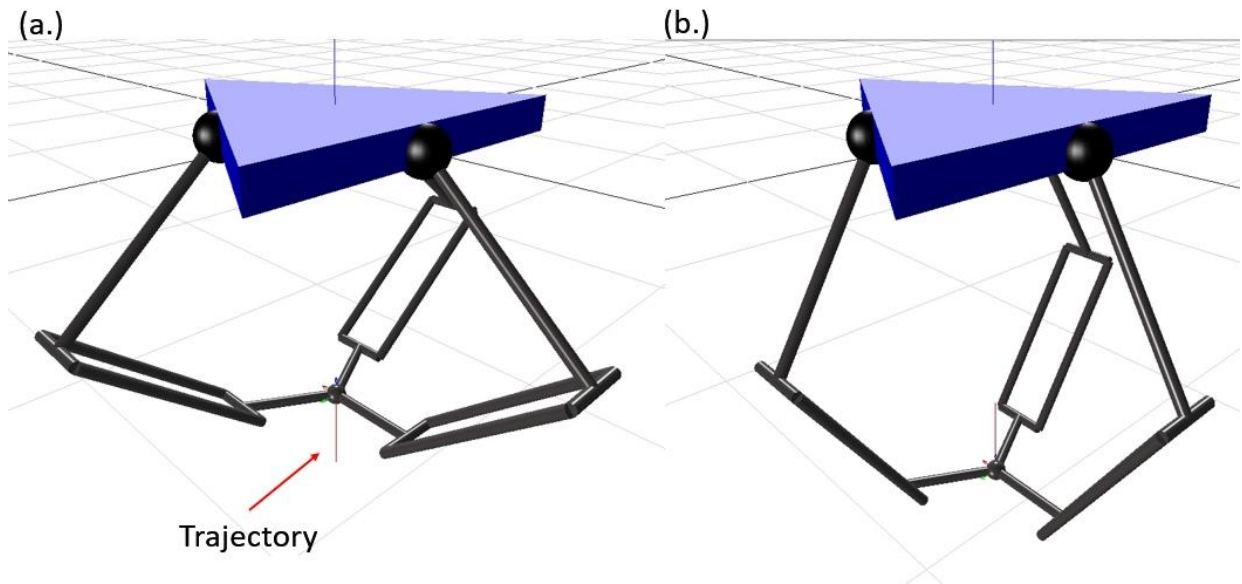


Figure 18: Medical parallel manipulator MapleSim model at initial and final configurations

Figure 19 shows the trajectory that the manipulator end-effector has followed. The manipulator demonstrated a sinusoidal motion with the displacement of 4.4 cm in Z-axis, which is within the recommended CPR depth range of 4 to 5 cm. There is a negligible error of 0.0002 cm offset in X-axis.

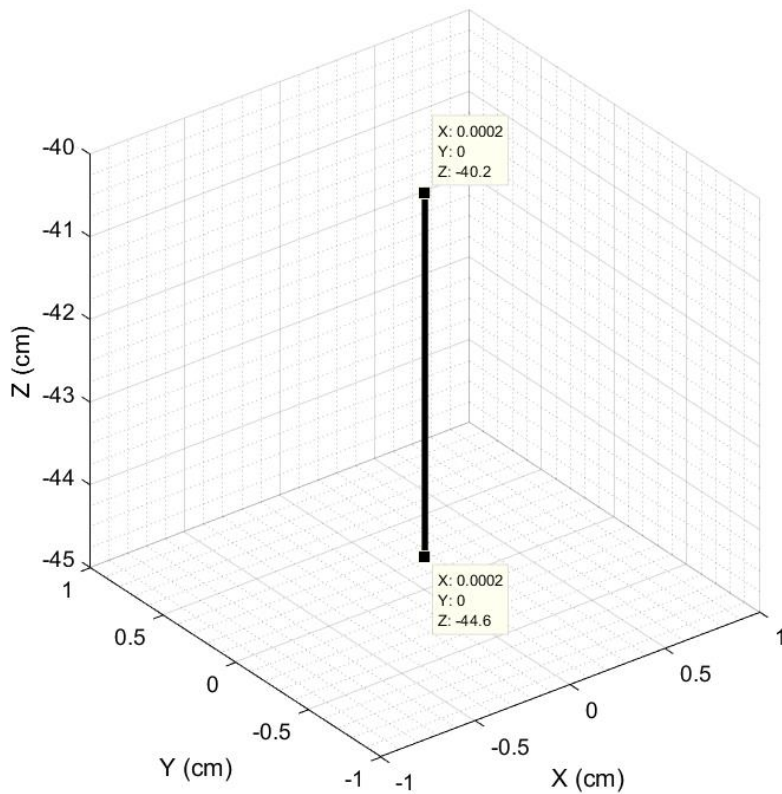


Figure 19: The trajectory of the mobile platform during the CPR operation

Figure 20 shows the displacement, velocity and acceleration of the end effector during the 60 seconds period. As expected, the displacement in X and Y axes are zero and the end effector oscillates in the Z axis. In addition, the Z-axis displacement waveform has 9 peaks indicating that 9 compressions are completed in 5 seconds and 108 compression in a minute, which is within the recommended CPR range of 100 – 120 cpm.

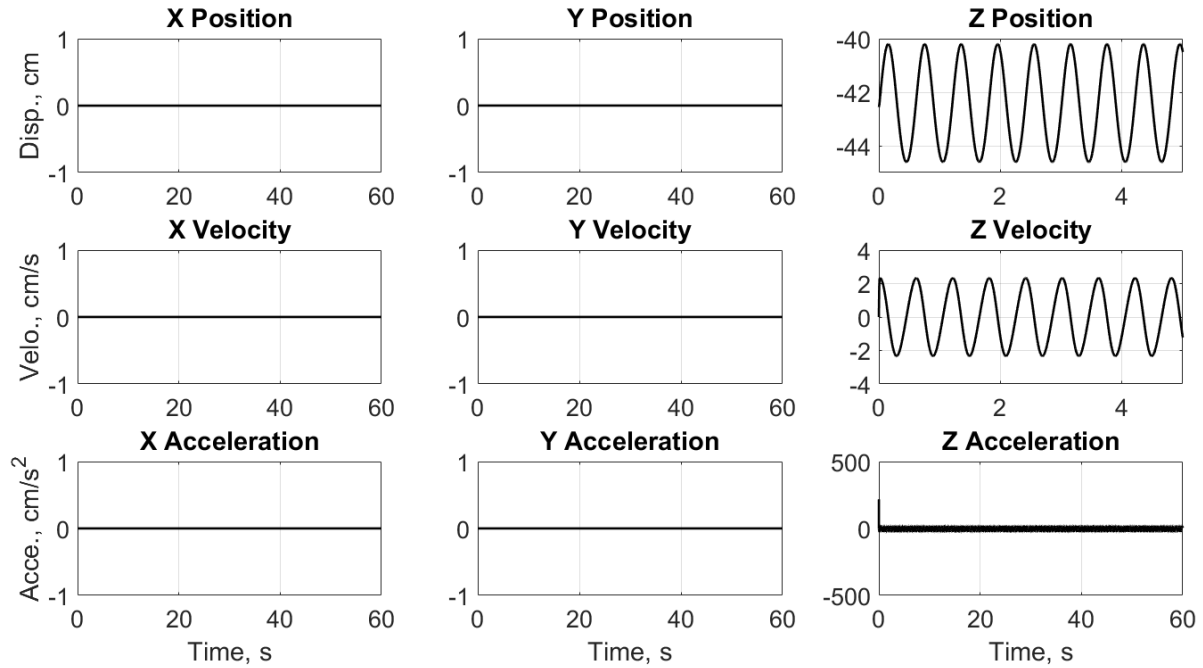


Figure 20: Displacement, velocity and acceleration of the mobile platform in X, Y and Z axes

ii. Mechanical Human Chest

In Chapter 3, the assumption was made to simplify the equation of motion defining the mechanical model of the human chest. According to the assumption, the moving mass of the chest m is relatively small compared to stiffness k and damping μ . Hence the effect of m was neglected. In this section, the human chest is modeled as a spring-damper system and the effect of different moving masses m is examined while the stiffness k and damping μ parameters were kept constant. As Figure 20 demonstrated, the motion is observed only in Z-axis. A prismatic joint allows a relative translation of the two connected frames in a single axis of motion. Therefore, the spring-damper system is modeled as a non-ideal prismatic joint with stiffness k and damping μ . *MapleSim* software provides a spring geometry block but it does not provide a 3D visual of a damper. Therefore, the spring-damper system is visualized by a spring, but it actually consists of both a damper and a spring. Figure 21 shows the *MapleSim* model of the mechanical human chest.

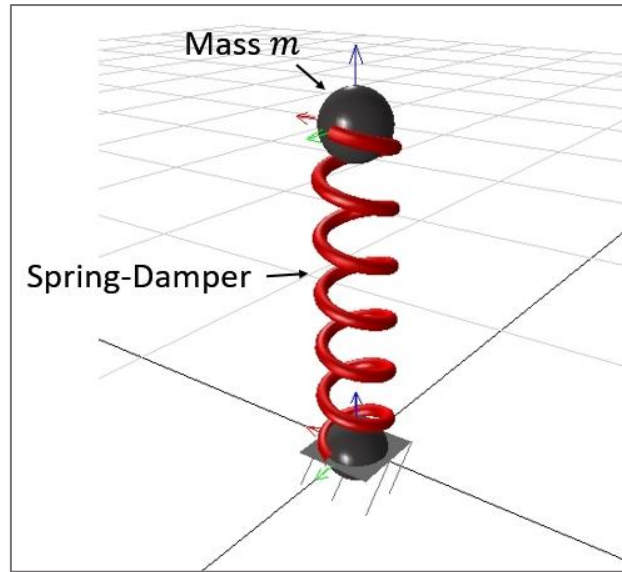


Figure 21: Human chest representation as a spring

According to [17], the average moving mass of the chest during chest compressions is 2.39 kg. Figure 22 demonstrates the effect of 1.39 kg change in m on the displacement. The steady state displacement of the system is 8.36 cm and the peak discrepancy between the two results is 0.183 cm. The steady state displacement is 4568.3% of the peak discrepancy, which indicates that assumption was accurate.

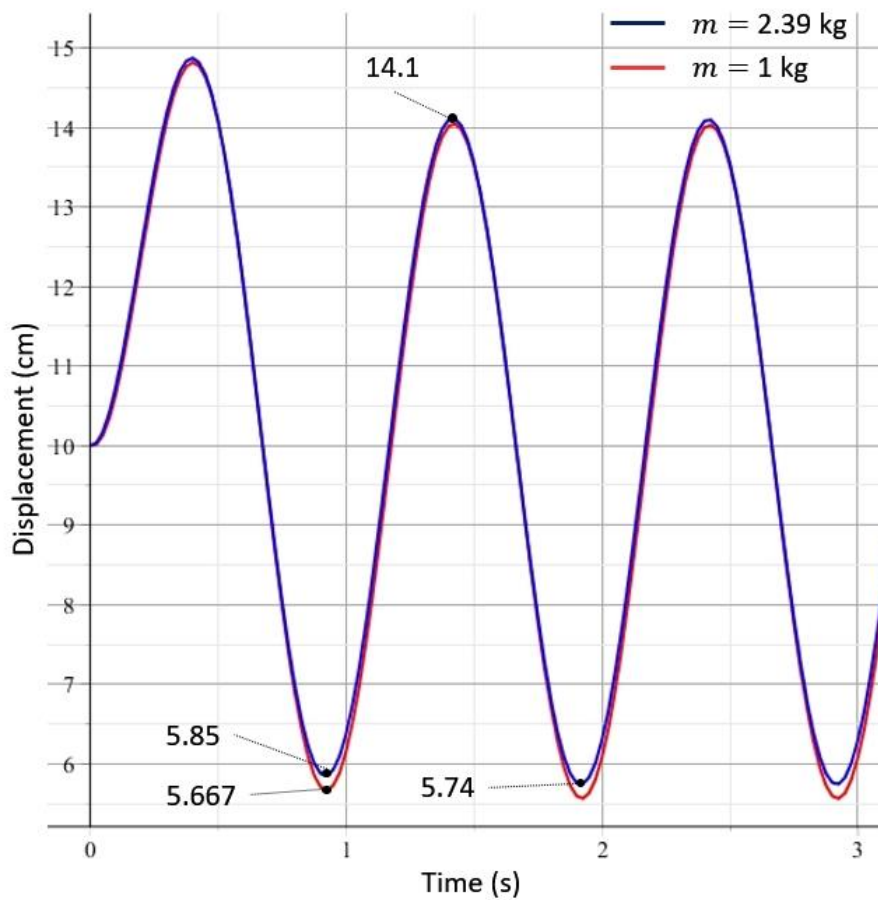


Figure 22: Comparison of two spring-damper systems with different masses

iii. 3-RRPaR Medical Manipulator Applied to a Mechanical Human Chest

In this section, the equations derived in Chapter 3 are used to calculate the parameters that are needed to model the human chest as a spring-damper system in the *MapleSim* environment. Then, the parallel manipulator model is used to perform chest compressions to the modeled human chest.

Table 4 demonstrates the chosen chest stiffness and chest damping values for experiments 1, 2, 3, and 4.

	Depth (cm)	Chest Stiffness (N/m)	Chest Damping (Ns/m)
Experiment 1	5	8500	500
Experiment 2 (PD Controller)	5	8500	500
Experiment 3	4	11250	300
Experiment 4 (PD Controller)	4	11250	300

Table 4: The stiffness and damping values used in experiments 1, 2, 3, and 4.

Figure 23 demonstrates the initial (a.) and final (b.) positions of the parallel manipulator, where the end-effector is attached to the human chest model (spring-damper system) illustrated by a spring.

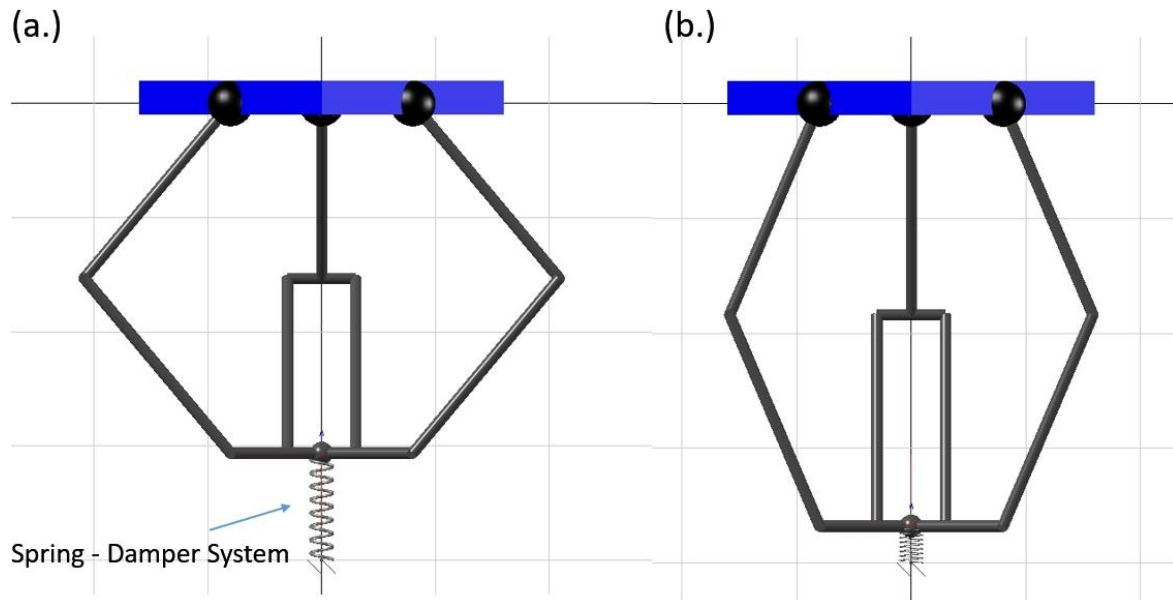


Figure 23: CPR performed on the mechanical chest model

Figure 24 shows the displacement of the moving base (end-effector) with respect to the human chest when chest stiffness and damping are 8500 N/m and 500 Ns/m, respectively. It can be seen that in the steady state region, the relative displacement settles at 5 cm, as expected.

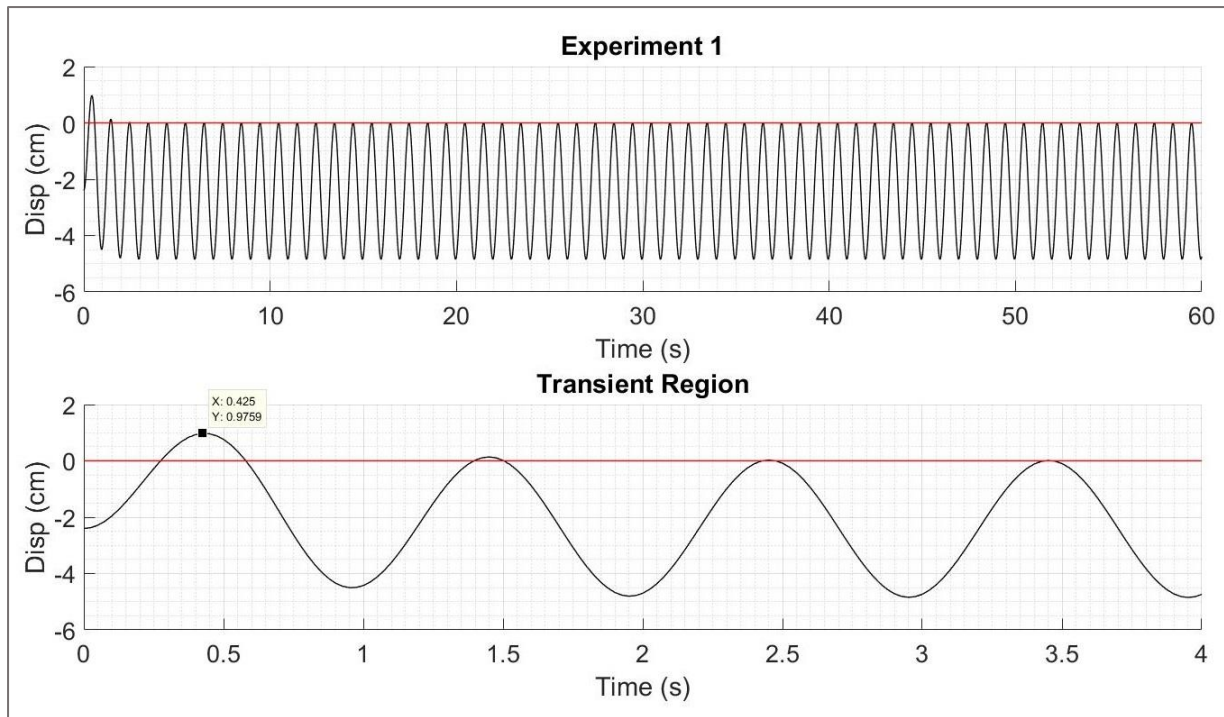


Figure 24: Simulation results of the chest model, $k=8500$ and $c=500$

Figure 25 shows the effect of the PD controller on the displacement of the moving base with respect to the human chest when chest stiffness and damping are 8500 N/m and 500 Ns/m, respectively. It can be seen that the spike in the initial transition from decompression to compression is reduced from 0.98 cm to 0.2 cm by the implementation of the PD controller.

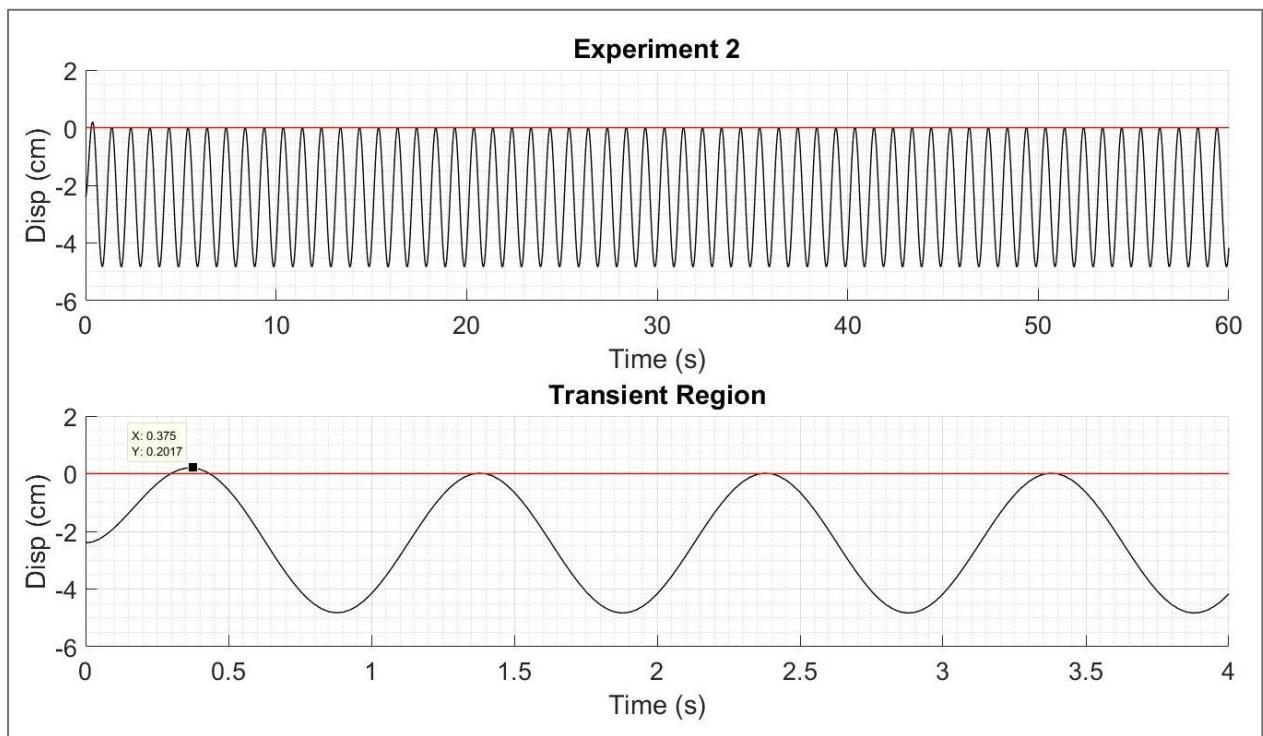


Figure 25: Simulation result using PD controller, $k=8500$ and $c=500$

Figure 26 shows the displacement of the moving base with respect to the human chest when chest stiffness and damping are 11250 N/m and 300 Ns/m, respectively. It can be seen that in the steady state region, the relative displacement settles at 4 cm, as expected.

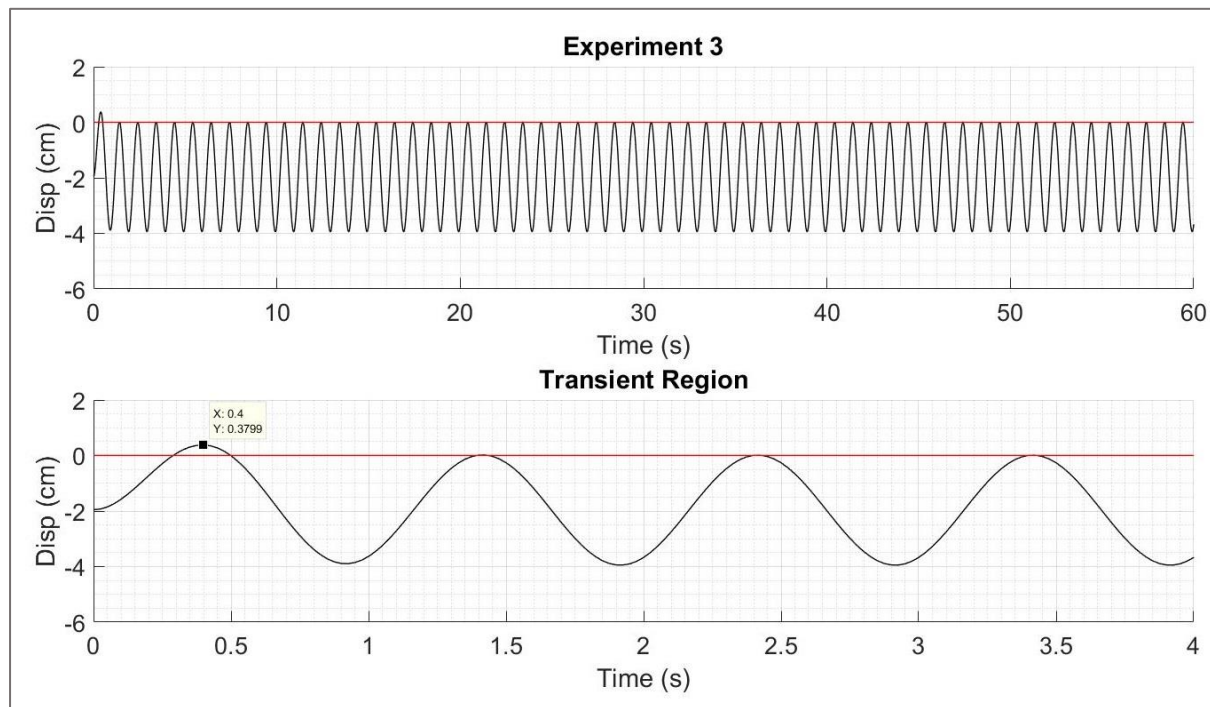


Figure 26: Simulation results of the Chest Model, $k=11250$ and $c=300$

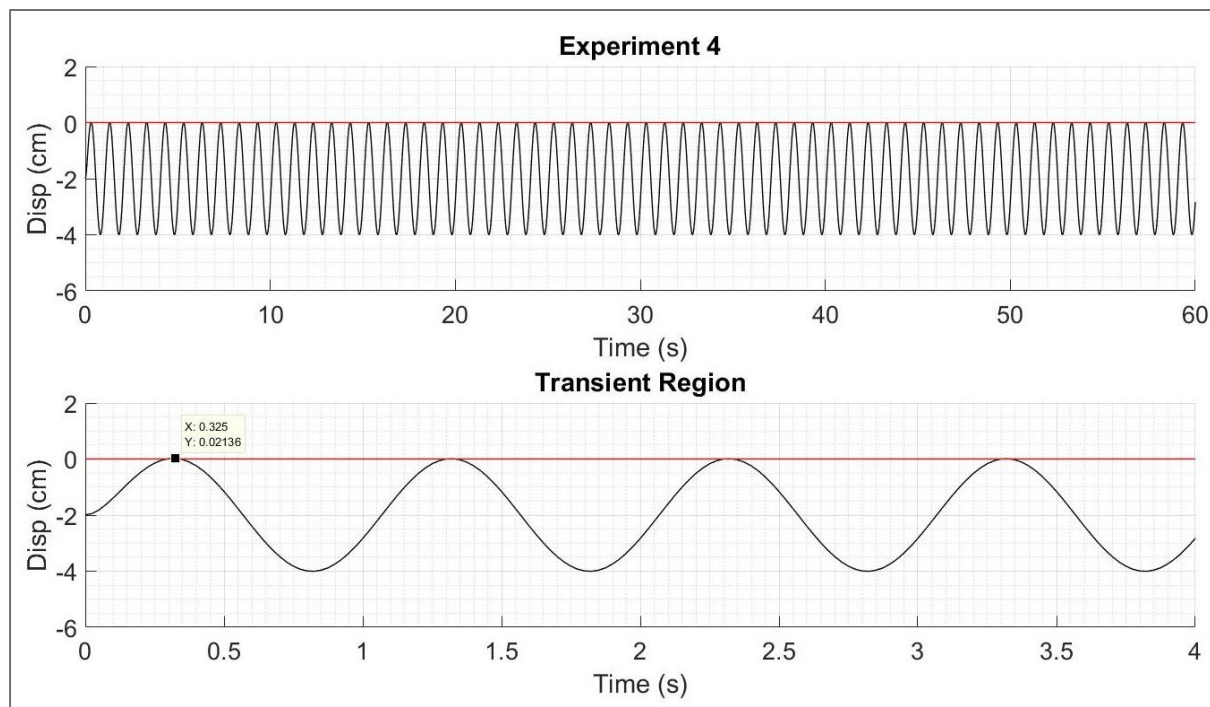


Figure 27: Simulation Results using PD controller, $k=11250$ and $c=300$

Figure 27 shows the effect of the PD controller on the displacement of the moving base with respect to the human chest when chest stiffness and damping are 11250 N/m and 300Ns/m,

respectively. It can be seen that the initial transition from decompression to compression is reduced from 0.38 cm to 0.0214 cm by the implementation of the PD controller.

6. Conclusion

In this paper, an alternative to the chest compression process of CPR operation was presented. Although a number of other alternatives are already available, the simulation results of the CT method implementation proved the high stiffness and high accuracy characteristics of the proposed conceptual design. The three reasons listed in Chapter 1 showed that the implementation of the proposed design in CPR operation is likely to reduce the risk and workload of doctors.

The inverse dynamic model of proposed 3-RRPaR manipulator was derived based on the virtual work principle by employing a few simplification hypothesis. Using the derived dynamic model, an implementation of dynamic control was established in joint space.

In future, two new control methodologies, e.g. fuzzy supervisory, and adaptive neuro-fuzzy inference system (ANFIS) maybe implemented to control the motion of the robot manipulator. The fuzzy supervisory control and ANFIS methods have an advantage over the PD control of computed torque method, as these two methods do not require the tuning of controller gains. In addition, one may focus on building a prototype of the proposed medical robot and implement the medical robot to assist in CPR operation.

7. References

- [1] "The American National Red Cross: CPR Steps," [Online]. Available: <http://www.redcross.org/take-a-class/cpr/performing-cpr/cpr-steps>. [Accessed 07 11 2017].
- [2] "CPR Statistics - American Heart Association," 03 09 2014. [Online]. Available: <https://goo.gl/dAXf2e>. [Accessed 07 11 2017].
- [3] T. McRae, "CPR Facts and Stats - American Heart Association," [Online]. Available: <https://goo.gl/UULPej>. [Accessed 07 11 2017].
- [4] M. D. Christian, M. Loutfy, L. C. McDonald, K. F. Martinez, M. Ofner, T. Wong, T. Wallington, W. L. Gold, B. Mederski, K. Green and D. E. Low, "Possible SARS Coronavirus Transmission during Cardiopulmonary Resuscitation," *Emerging Infectious Diseases*, vol. 10, no. 2, p. 287–293, 2004.
- [5] Y. Li and Q. Xu, "Design and Development of a Medical Parallel Robot for Cardiopulmonary Resuscitation," *IEEE Transactions on Mechatronics*, vol. 12, no. 2, pp. 265 - 273, 2017.
- [6] Y. D. Patel and P. M. George, "Parallel Manipulators Applications—A Survey," *Modern Mechanical Engineering*, vol. 2, pp. 57 - 64, 2012.
- [7] D. Stewart, "A Platform with Six Degrees of Freedom," *Proceedings of the Institution of Mechanical Engineers*, vol. 180, no. 1, pp. 371 - 386, 1965.
- [8] "RobotWorks: ABB IRB 940," RobotWorks, [Online]. Available: https://www.robots.com/pdfs/robots/irb-940_datasheet.pdf. [Accessed 25 11 2017].
- [9] "IRB 360 FlexPicker®," ABB, [Online]. Available: <http://new.abb.com/products/robotics/industrial-robots/irb-360>. [Accessed 25 11 2017].
- [10] *Müller Invests in Automation*, 2014.
- [11] J. P. Ornato and M. A. Peberdy, *Cardiopulmonary Resuscitation*, Totowa, New Jersey: Humana Press, 2005.
- [12] "How to perform CPR," Frontier Lifeline, [Online]. Available: <https://frontierlifeline.wordpress.com/category/emergency/>. [Accessed 07 11 2017].
- [13] Y. Li and Q. Xu, "Dynamic analysis of a modified DELTA parallel robot for cardiopulmonary resuscitation," in *Intelligent Robots and Systems*, Edmonton, Alta., Canada, 2005.
- [14] M. Asgari and M. A. Ardestani, "Dynamics and Improved Computed Torque Control of a Novel Medical Parallel Manipulator," *Mechanics in Medicine and Biology*, vol. 15, no. 4, p. 23, 2015.

- [15] M. W. Spong, S. Hutchinson and M. Vidyasagar, *Robot Modelling and Control*, John Wiley & Sons, INC..
- [16] G. Yedukondalu, A. Srinath and J. S. Kumar, "Mechanical Chest Compression with a Medical Parallel Manipulator for Cardiopulmonary Resuscitation," *The International Journal of Medical Robotics and Computer Assisted Surgery*, no. 11, pp. 448-457, 2015.
- [17] A. A. Stanley, S. K. Healey, M. R. Maltese and K. J. Kuchenbecker, "Recreating the Feel of the Human Chest in a CPR Manikin via Programmable Pneumatic Damping," in *IEEE Haptics Symposium*, 2012.
- [18] J. Nysaether and I. Rafoss, "Chest Simulator". United States of America Patent US 2007/0264621 A1, 15 11 2007.
- [19] A. Tomlinson, J. Nysaether, P. Steen, J. Kramer-Johansen and E. Dorph, "Compression force-depth relationship during out-of-hospital cardiopulmonary resuscitation," *Resuscitation*, vol. 72, pp. 364-370, 2007.
- [20] J. K. Russell, D. M. Gonzalez-Otero, S. R. d. Gauna, M. R. Daya and J. Ruiz, "Recoil and Release Times in Manual Chest," *Resuscitation*, vol. 18, no. 1, p. e30, 2017.
- [21] S. G. Beesems, B. M. Hardig, A. Nilsson and R. W. Koster, "Force and depth of mechanical chest compressions and their relation to chest height and gender in an out-of-hospital setting," *Resuscitation*, vol. 91, pp. 67-72, 2015.
- [22] B. Siciliano and O. Khatib, *Handbook of Robotics*, Springer , 2007.
- [23] J. J. Craig, *Introduction to Robotics: Mechanics and Control*, Addison-Wesley, 2009.
- [24] C. S. Gurel, "Research Gate," 13 10 2017. [Online]. Available: https://www.researchgate.net/publication/320386792_Hexapod_Modelling_Path_Planing_and_Control. [Accessed 26 11 2017].

8. Appendix

i. Additional Visuals of the Proposed Design

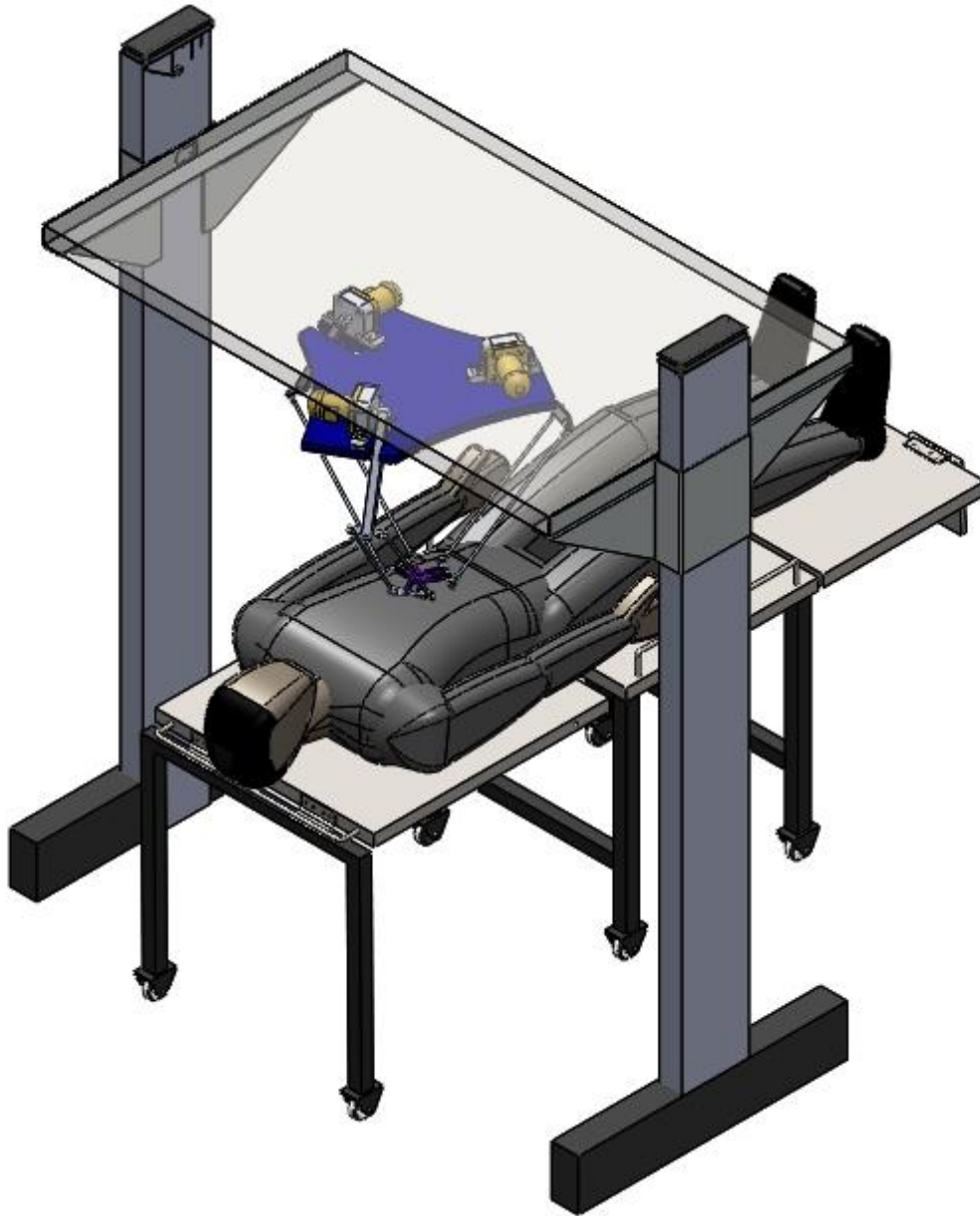


Figure 28: Additional visual 1 of the SolidWorks design

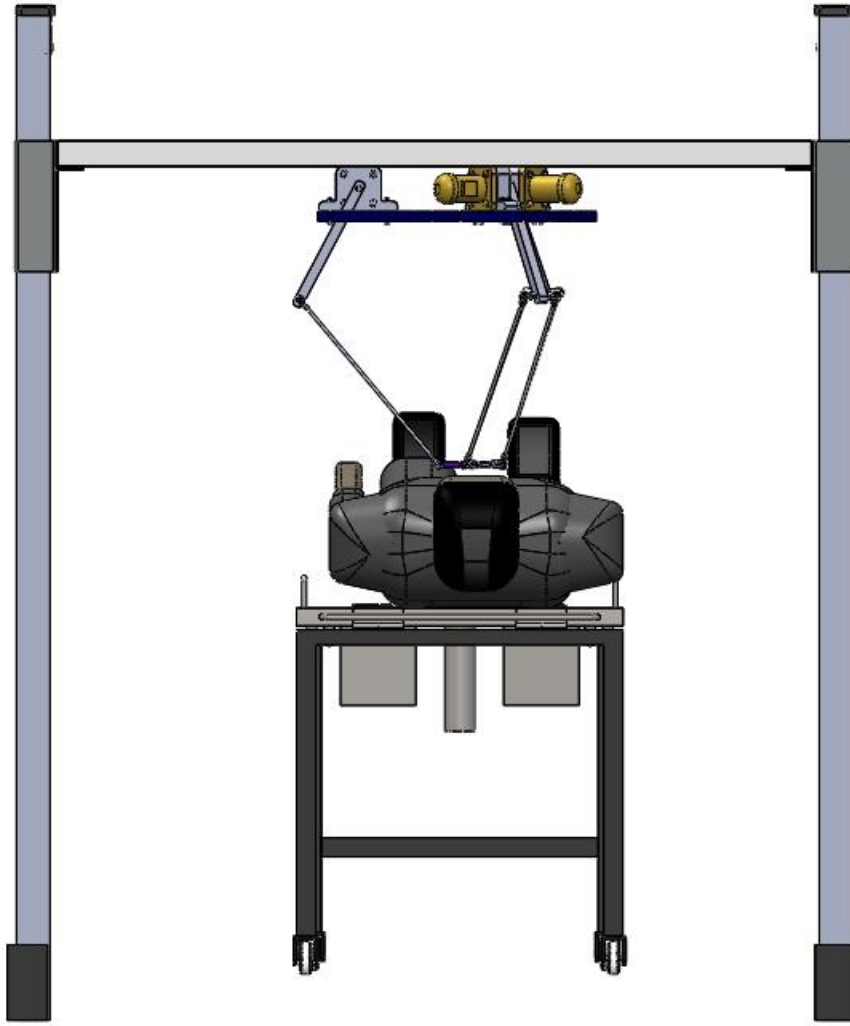


Figure 29: Additional visual 2 of the SolidWorks design

ii. Detailed Inverse Kinematics Calculations

Note that for simplicity, $\cos(\cdot)$ and $\sin(\cdot)$ have been aliased to $c(\cdot)$ and $s(\cdot)$, respectively.

Taking the square of the RHS of Equation 2.4,

$$c(\phi_i)^2 p_x^2 + 2 c(\phi_i) s(\phi_i) p_x p_y + 2(h-r)(\cos(\phi_i) p_x + \sin(\phi_i) p_y) + s(\phi_i)^2 p_y^2 + (h-r)^2 \quad (8.1)$$

Taking the square of the RHS of Equation 2.5,

$$s(\phi_i)^2 p_x^2 - 2 c(\phi_i) s(\phi_i) p_x p_y + c(\phi_i)^2 p_y^2 \quad (8.2)$$

Taking the square of the RHS of Equation 2.6,

$$p_z^2 \quad (8.3)$$

Adding Equations 8.1-8.3,

$$c(\phi_i)^2 p_x^2 + 2c(\phi_i) p_x(h-r) + s(\phi_i)^2 p_y^2 + 2s(\phi_i) p_y(h-r) + (h-r)^2 + s(\phi_i)^2 p_z^2 + c(\phi_i)^2 p_y^2 + p_z^2 \quad (8.4)$$

Factoring out p_x^2 and p_y^2 ,

$$(p_x^2 + p_y^2)(c(\phi_i)^2 + s(\phi_i)^2) + 2(h-r)(\cos(\phi_i) p_x + \sin(\phi_i) p_y) + (h-r)^2 + p_z^2 \quad (8.5)$$

Using the Trigonometric Identity: $\sin(u)^2 + \cos(u)^2 = 1$

$$p_x^2 + p_y^2 + p_z^2 + 2\cos(\phi_i) p_x(h-r) + 2\sin(\phi_i) p_y(h-r) + (h-r)^2 \quad (8.6)$$

Taking the square of the LHS of Equation 2.4,

$$a^2 c(q_{1i})^2 + 2a c(q_{1i}) b s(q_{3i}) c(q_{1i} + q_{2i}) + b^2 s(q_{3i})^2 c(q_{1i} + q_{2i})^2 \quad (8.7)$$

Taking the square of the LHS of Equation 2.5,

$$b^2 c(q_{3i})^2 \quad (8.8)$$

Taking the square of the LHS of Equation 2.6,

$$a^2 s(q_{1i})^2 + 2a s(q_{1i}) b s(q_{3i}) s(q_{1i} + q_{2i}) + b^2 s(q_{3i})^2 s(q_{1i} + q_{2i})^2 \quad (8.9)$$

Adding Equations 8.7-8.9 and factoring out the common terms,

$$a^2(s(q_{1i})^2 + c(q_{1i})^2) + 2ab s(q_{3i}) (c(q_{1i}) c(q_{1i} + q_{2i}) + s(q_{1i}) s(q_{1i} + q_{2i})) + b^2(s(q_{3i})^2 + c(q_{3i})^2) \quad (8.10)$$

Using the Trigonometric Identity: $\sin(u)^2 + \cos(u)^2 = 1$

$$a^2 + 2ab s(q_{3i}) (c(q_{1i}) c(q_{1i} + q_{2i}) + s(q_{1i}) s(q_{1i} + q_{2i})) + b^2 \quad (8.11)$$

Using the Trigonometric Identity: $\cos(u) \cos(v) + \sin(u) \sin(v) = \cos(u - v)$

$$a^2 + 2ab s(q_{3i}) c(q_{1i} - (q_{1i} + q_{2i})) + b^2 \quad (8.12)$$

Simplifying Equation 8.12,

$$a^2 + 2ab s(q_{3i}) c(-q_{2i}) + b^2 \quad (8.13)$$

Using the Trigonometric Identity: $\cos(-u) = \cos(u)$

$$a^2 + 2ab s(q_{3i}) c(q_{2i}) + b^2 \quad (8.14)$$

Equating the LHS and RHS of the sum of squares,

$$a^2 + 2ab s(q_{2i}) c(q_{2i}) + b^2 = p_x^2 + p_y^2 + p_z^2 + 2(h-r)(\cos(\phi_i) p_x + \sin(\phi_i) p_y) + (h-r)^2 \quad (8.15)$$

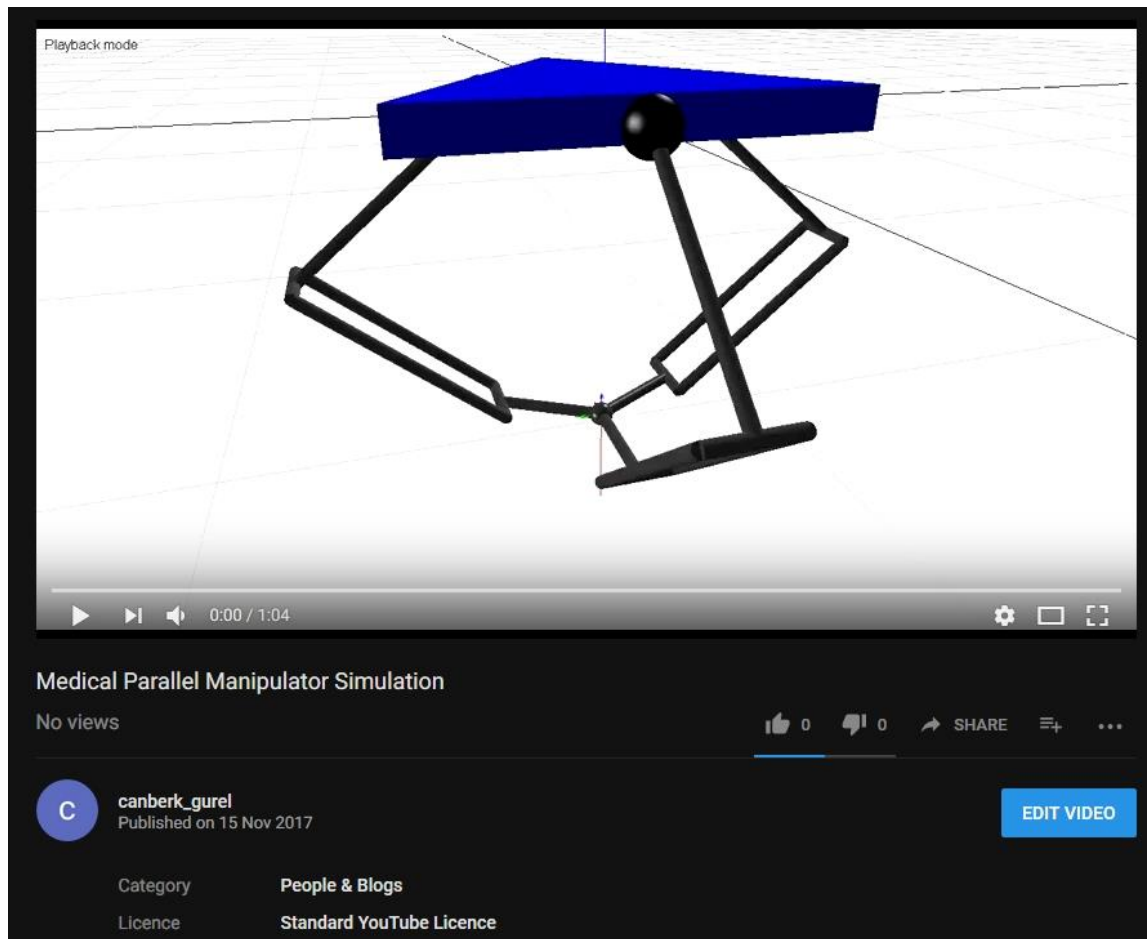
Solving for q_{2i} gives,

$$q_{2i} = \cos^{-1} \left(\frac{\text{Equation 8.6} - a^2 - b^2}{2ab \sin(q_{3i})} \right) \quad (8.16)$$

iii. Simplification Hypothesis

- ❖ The rotational inertias of the lower links are neglected.
- ❖ The mass of each lower link is evenly divided into two and concentrated at the endpoints B_i and C_i .
- ❖ The joints are frictionless.

iv. YouTube Video



<https://www.youtube.com/watch?v=jTgeUNiaHYA>

v. MapleSim and SolidWorks Files

Parallel manipulator simulation:

<https://drive.google.com/open?id=1jp-JLuJI5EqWzRluSjxLYWnbyP9w5b4>

Spring-damper simulation:

https://drive.google.com/open?id=16oe_AHPFRto3y6XW56lWO5ZAqv0XKN5c

Parallel manipulator and spring-damper system combined model:

<https://drive.google.com/open?id=1LnR9lUzQF-iBDJfVVC3Yo7tVqD0VJS9w>

Parallel Manipulator SolidWorks design:

<https://drive.google.com/open?id=1Er9KZya3xhaYWu--FOIZlCa0UQ4HJda3>